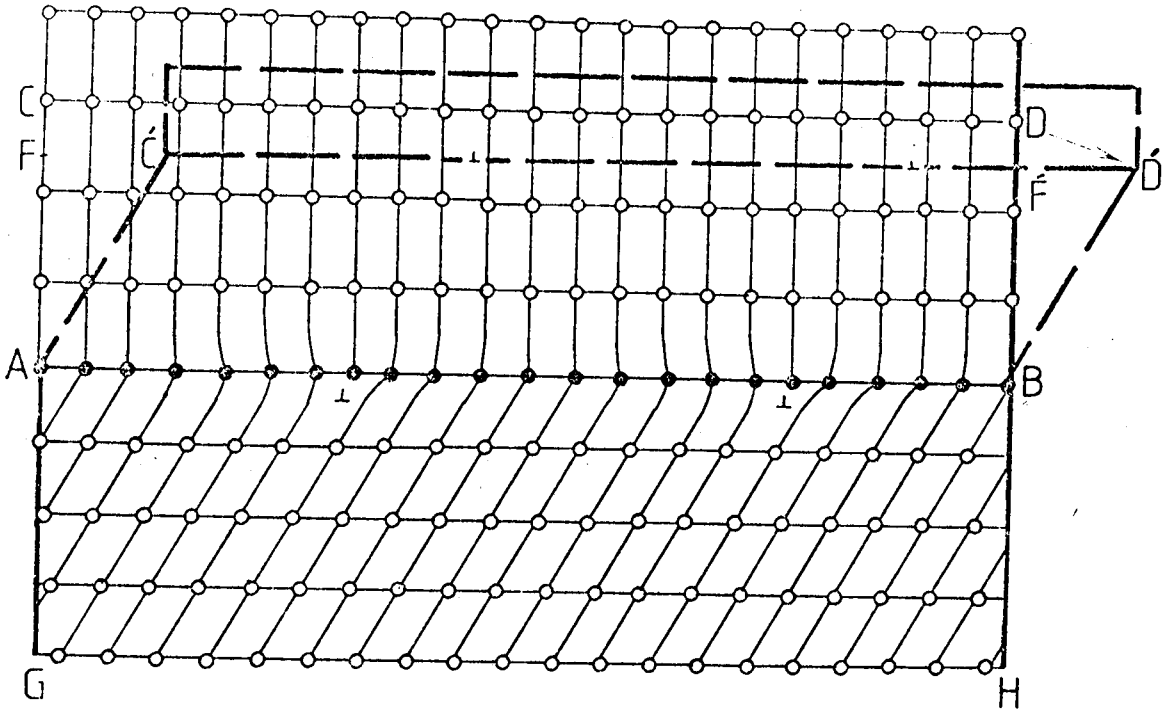


Figure 2.30. Diagram illustrating the nature of the shape change accompanying the movement of an epitaxially semi-coherent interphase interface. The dislocation climb implicit in the advance of AB to C'D' means that the new volume AC'D'B has a different number of atoms to the original ACDB. Diffusion normal to the interface plane is therefore required. In addition, a net flow parallel to the interface, i.e. from AFC' to BF'D', is likely destroying atomic correspondence and the shear component of the shape change.

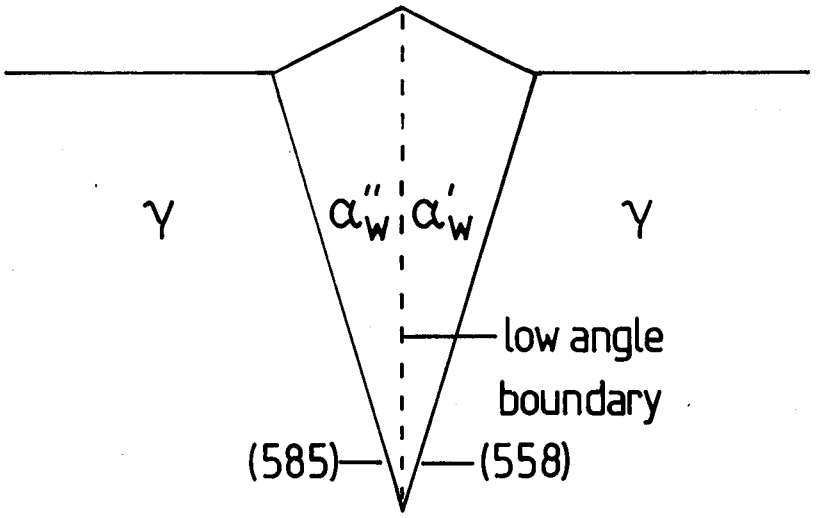


Figure 2.31. Schematic representation of Widmanstätten α.

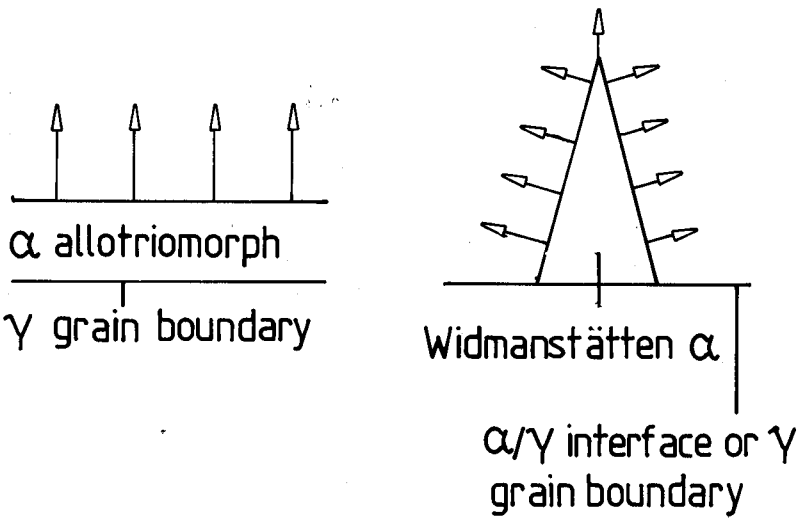


Figure 2.32. Comparison of point and planar diffusion.

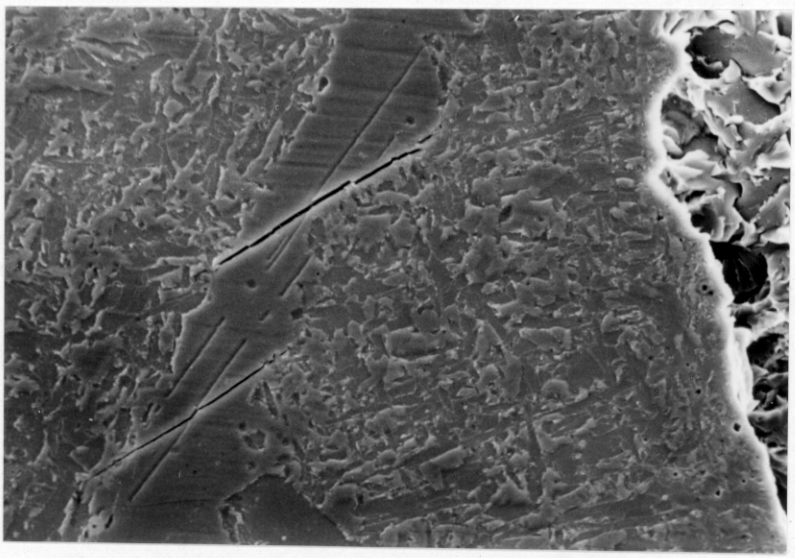

15μm

Figure 2.33. Cleavage crack in allotriomorphic α arrested by acicular ferrite [107].

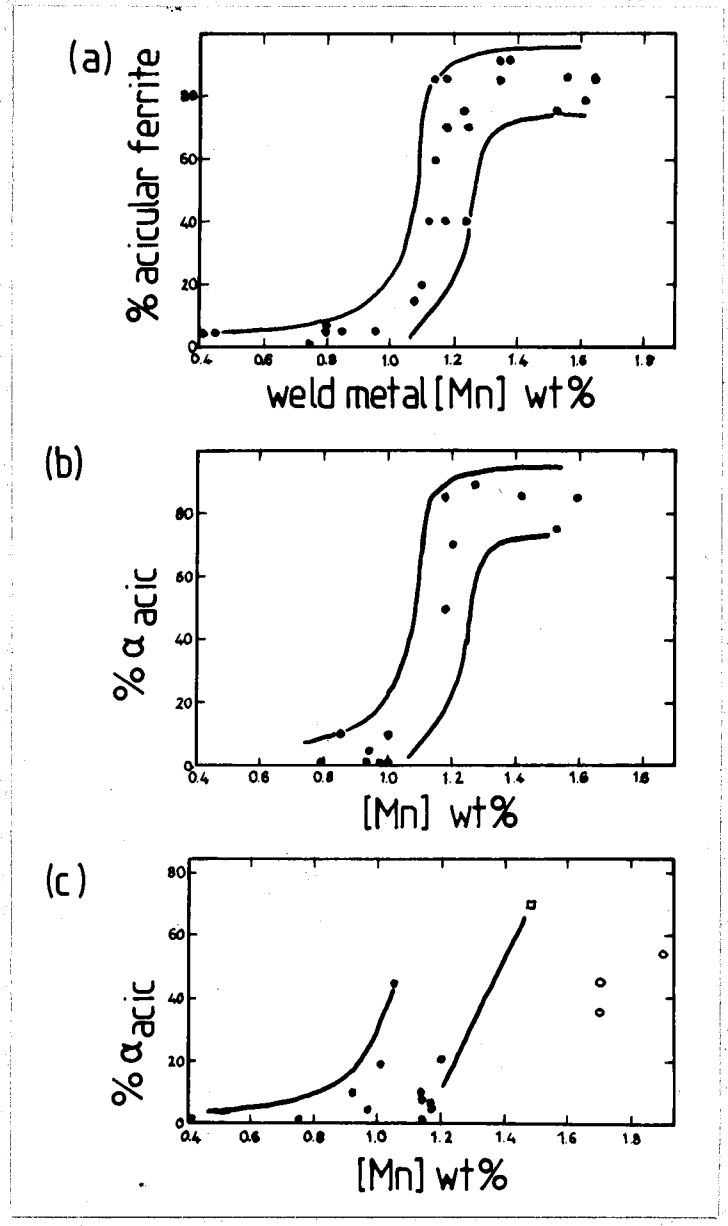


Figure 2.34. Variation of % acicular ferrite with weld metal manganese content[113].

(a) [O] < 400ppm

(b) 400 < [O] < 500ppm

(c) 500ppm < [O]

Farrar & Watson ●

Abson ○

Garland & Kirkwood □

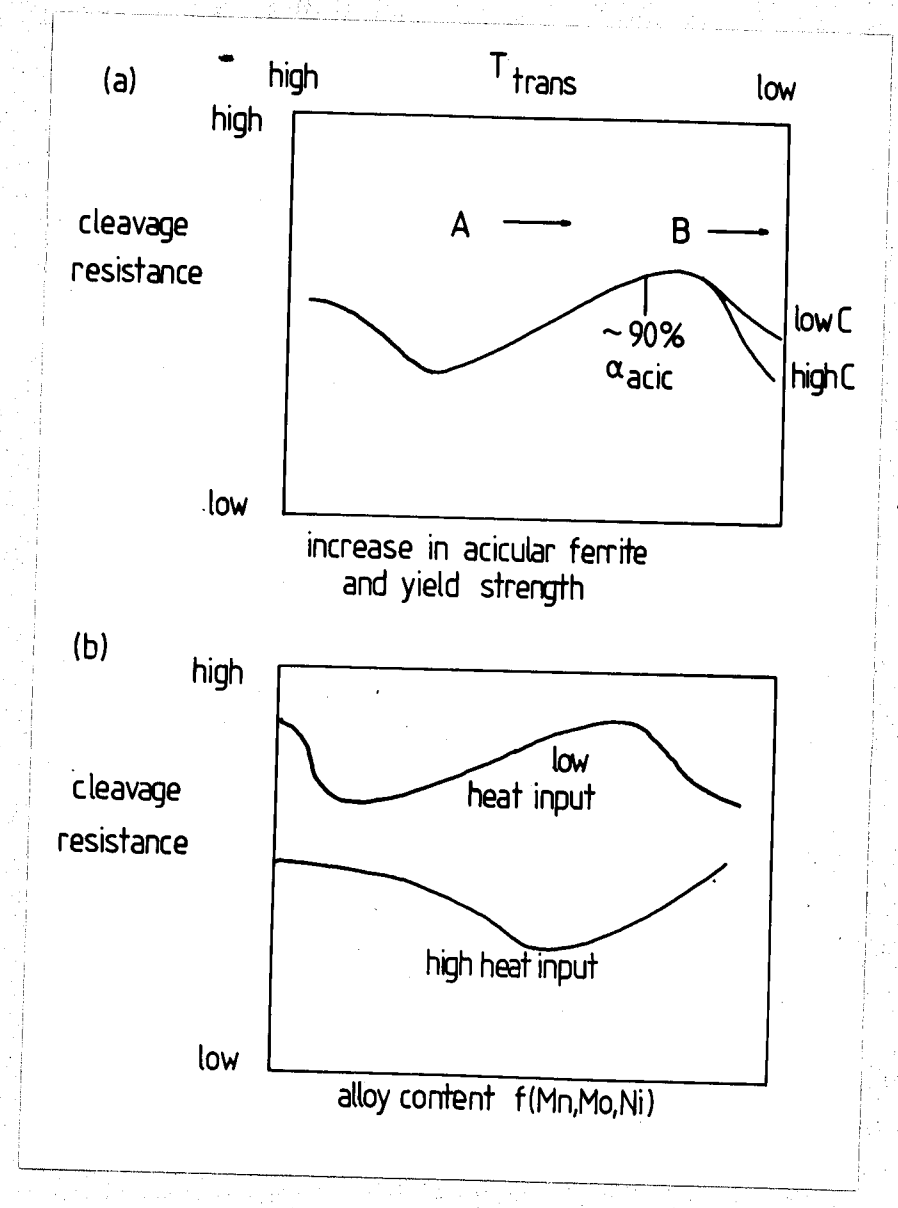


Figure 2.35. (a) Microstructure/cleavage resistance relationship.

A - decreasing allotriomorphic α and upper bainite

B - martensite formation

(b) Alloy/Cleavage resistance relationship. After Dolby [84].

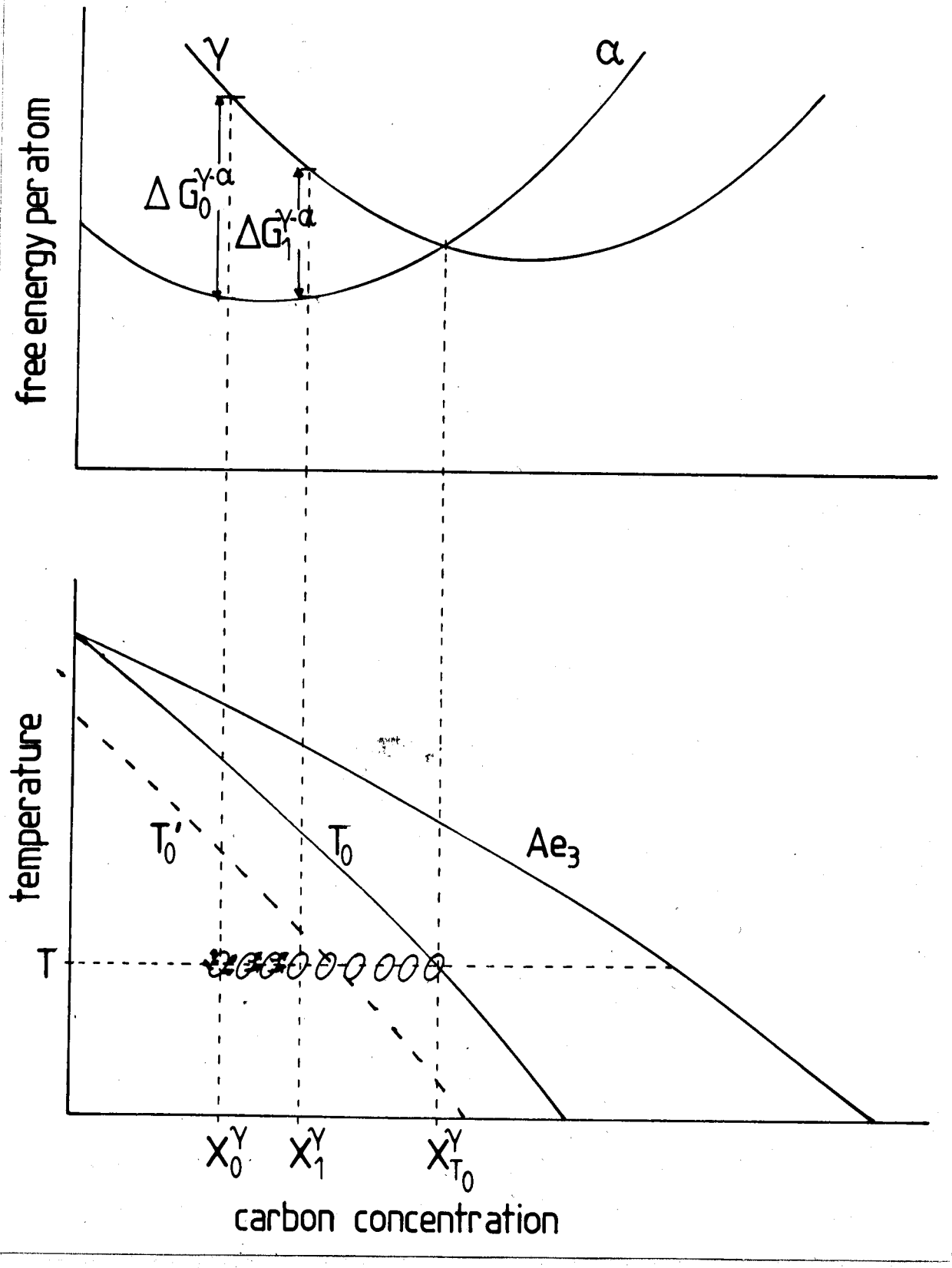


Figure 2.36. Formation of bainite and incomplete reaction.

0.3 μm

Figure 2.37. Lower bainitic carbides.

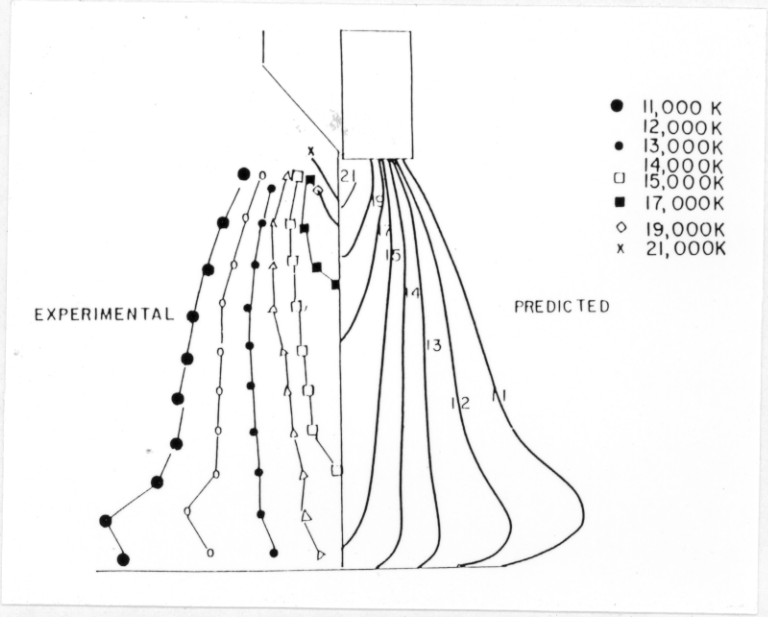


Figure 2.38. Comparison of predicted and measured arc isotherms[153].

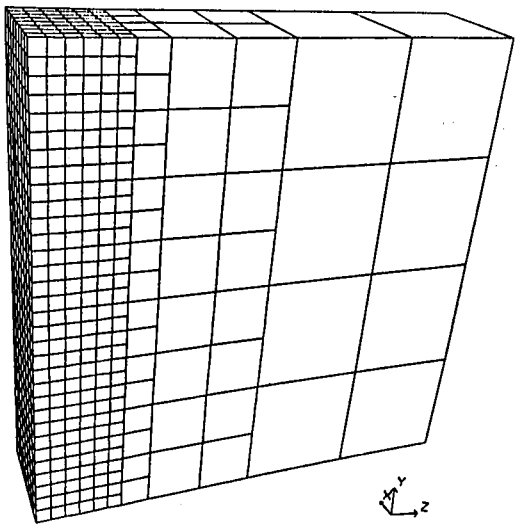

Figure 2.39. Graded finite element mesh, finer mesh nearer weld centreline[156].

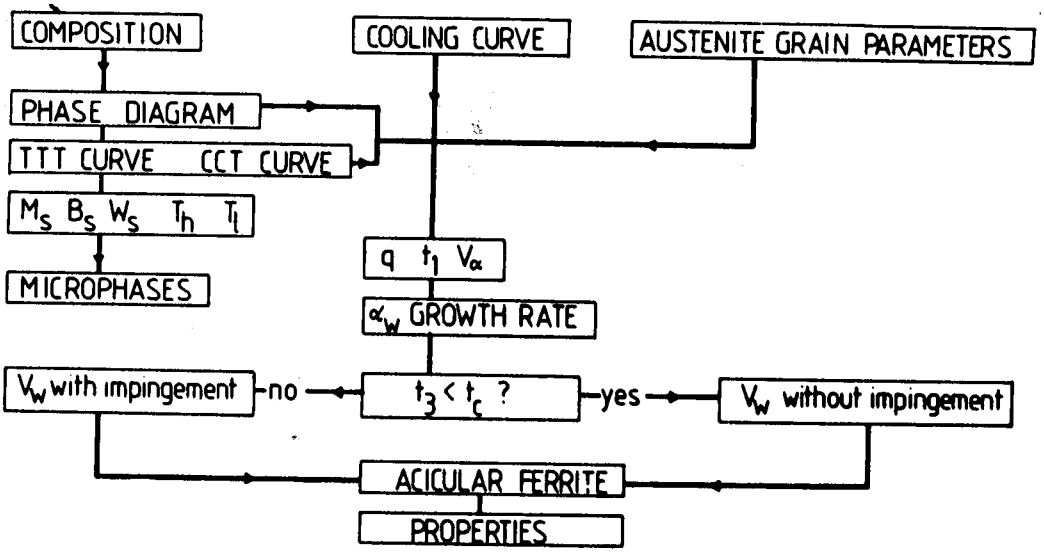


Figure 2.40. Flow diagram for BSG model.

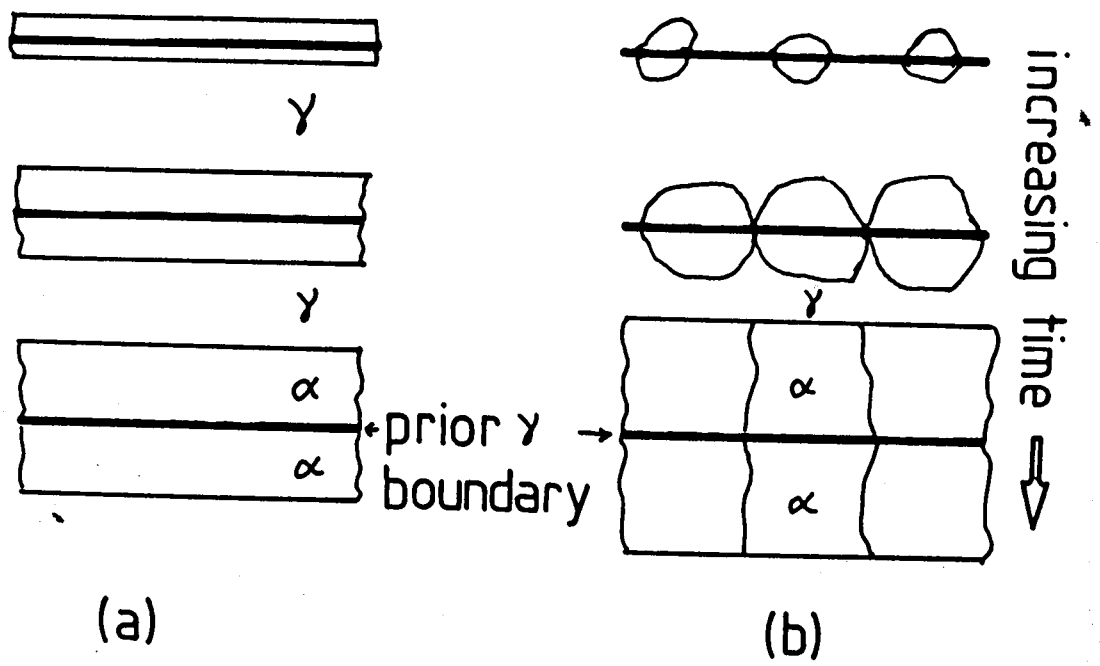


Figure 2.41. Comparison of α development as:

(i) a continuous grain boundary film;

(ii) separate allotriomorphs prior to impingement.

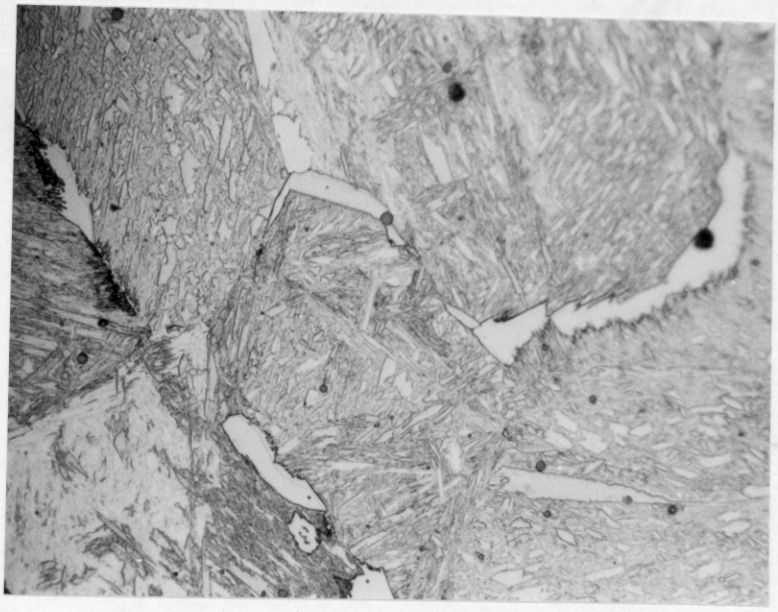

5.0 μm

Figure 2.42. Allotriomorphic α decorating prior γ grain boundaries.

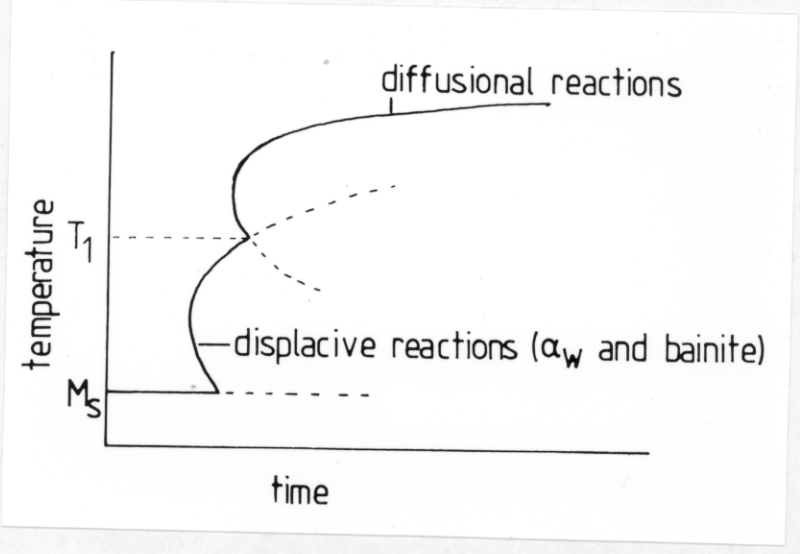


Figure 2.43. TTT curve illustrating $T_1$.

# 3. The Effect of Chemical Heterogeneities upon Ferrite Formation

## 3.1 Introduction and Theory

The growth rate of allotriomorphic ferrite can be accurately predicted for a variety of alloy compositions and undercoolings, but the extent of ferrite formation may vary with the degree of segregation. Variations in alloy content at grain boundaries compared with grain centres lead to a difference in the driving force for transformation ($\Delta G_V$), which may promote or hinder nucleation at the former sites. In addition to this nucleation effect segregation will have a strong effect on subsequent growth and final volume fraction of ferrite. This has important consequences in the prediction of weld metal microstructures. Bhadeshia [167] suggested that the effect of segregation would vary with undercooling and the theory proposed will be outlined here. In general, in a segregated specimen, ferrite will first form at grain boundaries deficient in substitutional alloying elements. The exact form of the composition profile is not important and can be represented as a sloping line on a composition/distance plot, (fig. 3.1), as opposed to the horizontal homogeneous line.

If grain boundary site saturation occurs, as in weld deposits where allotriomorphic ferrite completely decorates the prior $\gamma$ grain boundaries, then subsequent growth of ferrite will be by the normal advance of the planar $\gamma/\alpha$ interface into the grain. During this, carbon partition into the remaining $\gamma$ occurs ahead of the interface so that $\Delta G_V$ is decreased. Eventually, when the equilibrium volume fraction is achieved, the driving force is reduced to zero and interface motion ceases. Distances into the grain are given by $Z_{hom}$ for the homogeneous case and $Z_{het}$ for the heterogeneous specimen, substitutional alloying levels being represented by $X_{sh}$ and $X_{ss}$ for homogeneous and segregated cases respectively. This can also be studied by considering the distance into the grain at which motion ceases.

At low undercoolings, the volume fraction of ferrite formed in the homogeneous case is small and the interface is arrested a short distance $Z_{hom}$ into the grain (fig. 3.1a). At the corresponding point in the heterogeneous case $X_{ss}<X_{sh}$ so that the driving force for interface motion will be greater than zero. Therefore interface motion continues further into the grain eventually halting at $Z_{het}(>Z_{hom})$. This arises because the formation of a greater volume fraction of ferrite has resulted in greater carbon partition into the remaining $\gamma$ so reducing $\Delta G_V$ to zero. Thus at low undercoolings the volume fraction of ferrite formed in a heterogeneous sample would be expected to exceed that in the corresponding homogenised case.

The situation is reversed at high undercoolings where the volume fraction of ferrite is expected to be high. In the homogeneous situation (fig. 3.1b) the interface is arrested well into the grain ($Z_{hom}'$). In the heterogeneous specimen at the corresponding position $X_{ss}>X_{sh}$ so that the

driving force would have been reduced to zero at a lower carbon partition, i.e. at a smaller distance into the grain ($Z_{het}$'). This predicts that the volume fraction of ferrite formed in the latter case is less than that in the homogeneous case.

This analysis makes several assumptions concerning the governing transformation kinetics;

(i) Nucleation of ferrite occurs predominantly at grain boundaries, which for the heterogeneous case are solute-depleted.

(ii) Subsequent growth of ferrite is by the normal advance of the $\alpha/\gamma$ interface, i.e. the prior $\gamma$ grain boundaries are rapidly decorated by a continuous layer of ferrite.

(iii) Growth of ferrite allotriomorphs is reasonably rapid, i.e. by a NP-LE or ParaE (chapter 2) mechanism. This is necessary in order that the concentration gradient of the substitutional alloying element(s) is(are) not altered during the $\gamma$-$\alpha$ transformation. Hence, the decrease in $\Delta G_V$ is a result solely of carbon partition from the ferrite phase.

At all undercoolings the initial growth of ferrite in the segregated case is into an area depleted in alloying element compared with the homogeneous case and so would be expected to proceed at a faster rate than in the latter. In the later stages of the transformation (at higher undercoolings) ferrite growth rate will slow down as, in addition to carbon enrichment, solute rich regions are approached. The rate would then be less than that in the homogeneous case and a plot of rate versus time should show a crossover.

The fast ParaE growth rates, large scale segregation and variation of undercooling (through heat input) experienced during fusion welding make verification of this effect desirable as strong effects are noted on toughness through variations in grain boundary $\alpha$ width [83].

### 3.2 Experimental Verification

An earlier study [168] utilising low carbon steel gave ambiguous results due to transformation during the quench and so a higher alloy steel, A533B (Table III.1) was chosen for this work. This was available in the as-rolled, compositionally banded conditions and was machined to 3mm diameter rods, 20mm in length, parallel to the rolling direction. The banding wavelength was <<3mm so that these rods contained several composition cycles across the width. The mean composition of the rods was also then the bulk composition. Homogenised specimens were prepared by sealing in quartz tube under a partial pressure of argon followed by 3 days at 1200°C. Following this, substitutional alloy element levels in both homogeneous and segregated samples were determined by energy dispersive spectroscopy (EDS) techniques on an ISI-100A scanning electron microscope with Link 860 series II attachment, (Table III.2). Transformation at a series of undercoolings was studied using a Theta Industries high speed dilatometer, which allows the progress of the transformation to be studied by measuring the length change of a cylindrical specimen as a function of time at temperature (fig. 3.2).

*3.2.1 Theta Industries High Speed Dilatometer*

A large amount of dilatometry was undertaken during this project and so this apparatus will be described in detail.

The cylindrical specimen has a Pt/Pt-10%Rh thermocouple spot welded to its surface near the centre to record the temperature experienced. The specimen is held between two quartz tubes one of which is fixed, whilst the second is attached to a linear transducer, which records any length change. A quartz sleeve surrounds the specimen separating it from the radio frequency (RF) induction coil and preventing transfer of material from specimen to coil, which would affect coil performance. The linear transducer was calibrated over the temperature range used, using a pure platinum specimen of accurately known thermal expansivity, which was compared with that obtained from the dilatometer.

Each specimen was set up in the dilatometer as follows:

(i) Specimen placed between quartz tubes so that all three are colinear, surrounded by quartz sleeve and slid inside coil.

(ii) Thermocouple connected to recorder contacts and helium line fixed onto quartz tube.

(iii) Transducer 'tuned' using micrometer, for desired magnification, so that the length change recorded is not magnification dependent.

(iv) Lid fitted, chamber pumped down to 75μm Hg, then back filled with a partial pressure of helium to reduce decarburisation effects. Temperature (T) and length change (ΔL) zeroed on recorders.

(v) Specimen heated to reaustenitising temperature ($T_\gamma$) at a linear rate, controlled by Data-Trak programmer.

(vi) Austenitised for a set time, then helium quenched to the isothermal treatment temperature for a set time before quenching to room temperature.

The output is recorded on a Honeywell chart recorder as temperature vs time (distance along chart) and length change vs time.

*3.2.2 Isothermal Treatments*

The RF heating coil employed is a heat source of near-zero thermal mass and hence gives very quick temperature changes, this being complemented by helium quenching to give very rapid cooling so that quenching to the isothermal temperature can be achieved without transformation beginning. In order to reduce nucleation at the free surface, as this analysis applies to grain boundary nucleation, the specimens were Ni plated[1] as this has been found to be highly effective in suppressing α nucleation (see chapter 7) at the free surface. The specimens were reaustenitised

---

1 A two stage treatment
Strike:3 minutes at 50°C, 775mAcm$^{-2}$; electrolyte 250g $NiSO_4$+27ml conc. $H_2SO_4$ made up to 1 litre in distilled water.
Plate:25 minutes at 35°C, 40mAcm$^{-2}$; electrolyte 140g $NiSO_4$+15g $NH_4Cl$+20g Boric acid made up to 1 litre in distilled water.

at 1000°C for 10 mins; this was kept constant for all specimens to ensure constant $\gamma$ grain size. A balanced $\gamma$ grain size was required, as a large grain size may lead to the formation of intragranular products, but too fine a grain size gives soft impingement of diffusion fields and may also lead to transformation during the quench. The specimens were then helium quenched to isothermal temperatures between 400°C and 730°C and held until transformation stopped. No specimens were held longer than three hours as, at longer times, substitutional alloying element redistribution may take place, which would invalidate the analysis. Final volume fractions of ferrite formed were determined dilatometrically from the overall length change and confirmed by area fraction measurements on a Quantimet 720. If the length change is $\Delta L$ at temperature T, then assuming the volume change is isotropic, the length change and volume change are equal:

$$\Delta L/L_0=\Delta V/V \qquad .....(37)$$

Considering one austenite unit cell, its new volume ($V_{uc}$) is:

$$V_{uc}=\frac{3\Delta L a_\gamma^3}{L_0}+a_\gamma^3 \qquad .....(38)$$

$a_\gamma$=initial austenite lattice parameter at T

The initial austenite lattice parameter is calculated from the equations of Dyson and Holmes [169], accounting for alloy content and thermal expansivity. Two equations exist for estimating $a_\gamma$:

$$a_\gamma=3.555+0.44x_C^\gamma \qquad .....(39)$$

$$a_\gamma=3.573+0.33x_C^\gamma \qquad .....(40)$$

$x_C^\gamma$=mole fraction of carbon in austenite

Initially, $V_{uc}$ was calculated using both values, but, from a comparison of dilatometric and optical measurements of the volume fraction of ferrite ($V_\alpha$), equation 39 was found to be more accurate.

The new volume of an austenite unit cell can also be calculated from changes in the lattice parameters due to formation of ferrite and from partition of carbon into the remaining austenite. The partition of carbon causes an expansion in $a_\gamma$ and the degree of partition depends upon temperature, i.e. the equilibrium carbon level in ferrite, and the volume fraction of ferrite formed. If $a_\alpha$ is the lattice parameter of ferrite and $a_\gamma'$ that of austenite after partition of carbon, the volume of a former austenite unit cell is:

$$V_{uc}=2V_\alpha a_\alpha^3+(1-V_\alpha)a_\gamma'^3 \qquad .....(41)$$

The factor 2 arises from the fact that each FCC unit cell contains four atoms and so is equivalent to 2 BCC unit cells.

The ferrite lattice parameter was measured by Debye-Scherrer powder diffraction methods with the $a_\alpha$ values from each value of $\Theta_b$ (the Bragg angle) being extrapolated to $\Theta_b=90°$ to give the most accurate value for $a_\alpha$. The specimen was prepared by ageing at 500°C for 24 hours to fully form ferrite and relieve as much stress as possible. After furnace cooling, rods 0.5x0.5x10.0mm were slit, under flood lubrication, from the aged block. Any deformed surface layer was removed prior to X-ray examination by etching for 0.5-2.0 minutes in an aqueous solution of 10%(by

volume) HF - 10% $H_2O_2$.

Iteration, using a Newton-Raphson approach, of $V_\alpha$ leads to the volume fraction of ferrite that gives equal values for $V_{uc}$ in equations 38 and 41, and so is that formed during the heat treatment.

The Quantimet was later used for particle counting studies.

### 3.3 Volume Fraction Variations

Fig 3.3 illustrates the variation of $V_\alpha$ with isothermal temperature for the two cases over the range studied and shows the general trends expected. At low undercoolings (T=650-750°C) a greater volume fraction of ferrite was obtained in the segregated specimens compared with the homogeneous case. On decreasing temperature both volume fractions increased but the difference between them decreased until a crossover at 650°C. A typical $V_\alpha$/time trace at a temperature above 650°C is shown in fig. 3.4 and indicates that the initial growth rate for a segregated specimen exceeds that for the homogeneous one.

Below 650°C (i.e. high undercoolings) a smaller volume fraction of ferrite was observed for the segregated case than for the homogeneous one. Again this is as predicted, but the actual volume fractions decreased instead of continuing to increase. The dilatometric values were confirmed by the Quantimet, so the decrease in $V_\alpha$ was not due to other transformations such as carbide precipitation affecting the recorded length change. Additionally, analysis of the growth rate, fig. 3.5, indicates that the initial growth rate in the segregated specimen was exceeded by that in the homogeneous one in this temperature regime. The microstructures in the two cases are shown in fig. 3.6 and reveal a change in morphology and distribution of the ferrite allotriomorphs. The segregated specimen (fig. 3.6a) has ferrite concentrated in bands along the prior $\gamma/\gamma$ grain boundaries, whereas it occurs in a more elongated form throughout the homogenised grains. Particle counting on a 3mm diameter section of each specimen (fig. 3.7) shows that the homogenised specimen contained more allotriomorphs (despite their changed morphology), which had developed to a greater size than those in the heterogeneous case. This suggests that nucleation is playing a great part in determining $V_\alpha$ at higher undercoolings, probably due to the much reduced growth rate at these temperatures. This will have further implications on the analysis, namely that the slow growth rate may allow some redistribution of substitutional alloying elements causing a variation in the composition (and hence driving force for $\gamma$-$\alpha$ transformation) plots, fig. 3.1. In addition, the occurrence of nucleation away from the grain boundaries and discrete grain boundary allotriomorphs means that growth is not solely by the normal advance of the $\alpha/\gamma$ interface into the prior $\gamma$ grains. Thus the volume fraction of ferrite cannot be simply related to the distance into the grain at which interface motion ceases. The very slow growth rate may also account for the decrease in $V_\alpha$ as the heat treatment may have been insufficient to fully develop this. Attempts to extend the treatment would invalidate the earlier analysis as this would allow partition of substitutional alloying elements to take place which

changes the segregation profile and will introduce further complex effects into the analysis.

Consideration of the critical free energy for nucleation ($\Delta G^*$) across a grain (fig. 3.8) and comparison with driving force at high and low undercoolings demonstrates the possible role of nucleation. At low $\Delta T$, the driving force for transformation is low and only exceeds $\Delta G^*$ in the vicinity of the boundaries in both cases, the effect of segregation being to enhance nucleation and initial growth rate, as observed at T=650-750°C. The driving force for transformation at higher $\Delta T$ is much greater and this is able to exceed $\Delta G^*$ throughout the grain leading to much more widespread nucleation. Nucleation in the segregated specimen is still restricted to the grain boundaries due to the higher alloy content in the grain centres and so the analysis is still valid in these specimens, but not in the homogeneous ones.

### 3.4 Conclusions

The prediction of variation of segregation effect was found to be correct at low undercoolings, where nucleation is limited to grain boundaries and the growth rates in homogeneous and segregated specimens are similar. However, as undercooling increases the resulting acceleration in nucleation rate causes deviations from the prediction when growth effects are masked as nucleation moves away from the grain boundary. The temperature at which this breakdown occurs is dependent on the level of segregation (i.e. the amplitude of the composition waves) and hence upon the alloy content. Therefore, the statement that the exact nature of the composition variation is not relevant is not valid when nucleation plays a role. The effect of segregation will also be dependent on the growth rate as at slow growth rates where partition will change the composition variation of the substitutional element. The prediction is most valid for small $V_\alpha$ forming under ParaE or NP-LE conditions and will be most prominent at high segregation levels. These conditions apply during fusion welding of low alloy steel weld deposits where ParaE ferrite growth occurs in a highly compositionally heterogeneous material. This could help account for some of the deviation between calculated and observed $V_\alpha$ in the BSG model, as this underestimates the volume fraction of allotriomorphic ferrite, but considers growth in an homogeneous system. The analysis will apply to weld deposits more than the specimens studied here as grain boundary nucleation of allotriomorphic ferrite occurs very rapidly and in preference to other nucleation sites in the interior of $\gamma$ grains. The assumptions of normal ParaE advance of the $\alpha/\gamma$ interface are valid as the conditions favour this growth mode, but the effect of continuous cooling needs to be incorporated.

Table III.1. Bulk composition of A533B (wt%).

| C | Mn | Ni | Mo | Si | Cu | Al | Cr | P | S | As | Sn |
|---|---|---|---|---|---|---|---|---|---|---|---|
| 0.25 | 1.51 | 0.63 | 0.53 | 0.22 | 0.04 | 0.02 | 0.06 | 0.005 | 0.005 | 0.025 | 0.005 |

Table III.2. Compositional variations in banding of as-received material (wt%).

| Region | Fe | Mn | Ni | Mo | Cr | Si | Al | Cu |
|---|---|---|---|---|---|---|---|---|
| Band | 95.4 | 2.2 | 0.8 | 0.7 | 0.2 | 0.5 | 0.1 | 0.1 |
| Matrix | 96.0 | 1.7 | 0.4 | 0.5 | 0.2 | 0.4 | 0.2 | 0.2 |

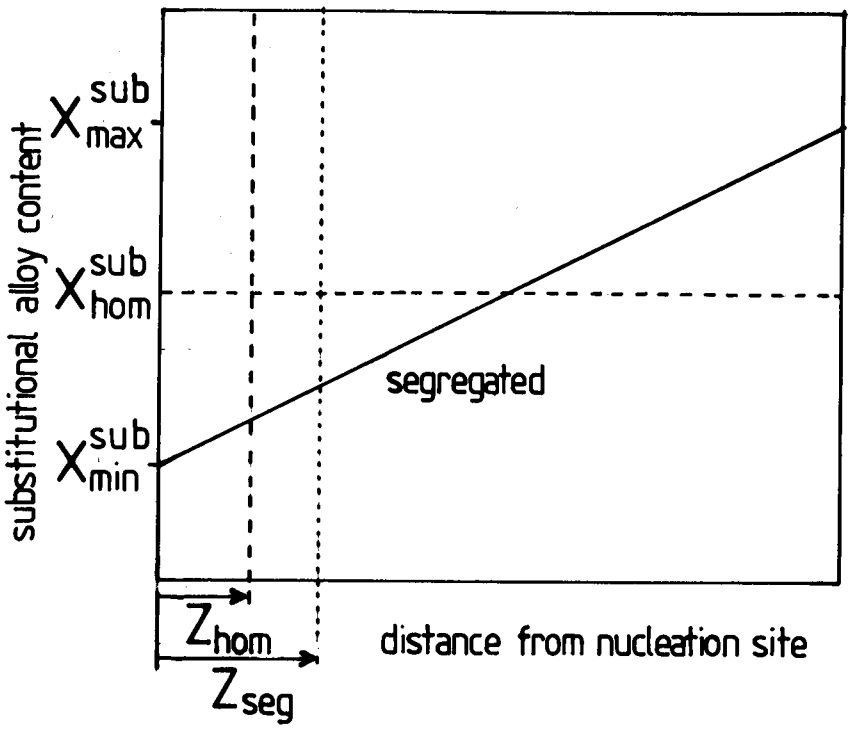


(a)

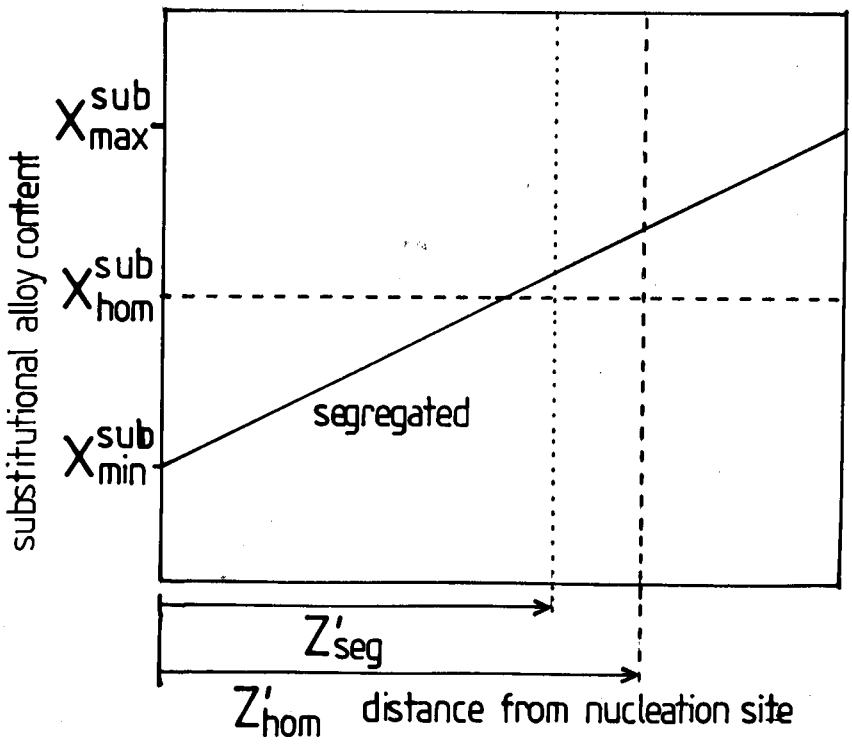


(b)

Figure 3.1. Composition/distance plots and interface arrest distances for segregated and homogeneous specimens, (a) low undercooling, (b) high undercooling.

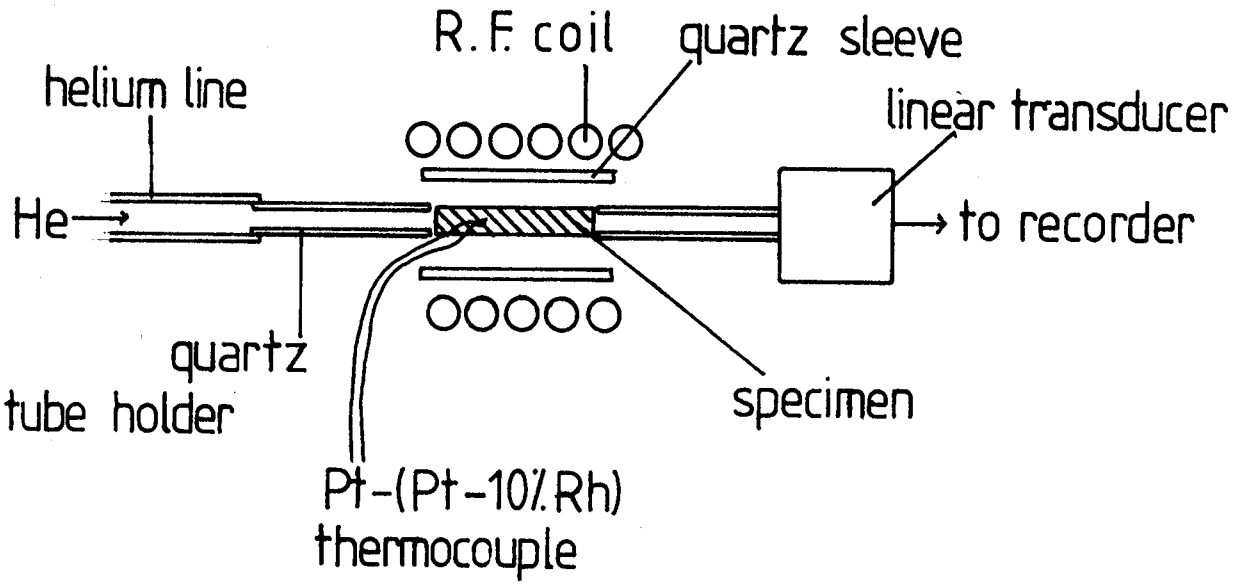


Figure 3.2. Schematic representation of dilatometer specimen set-up.

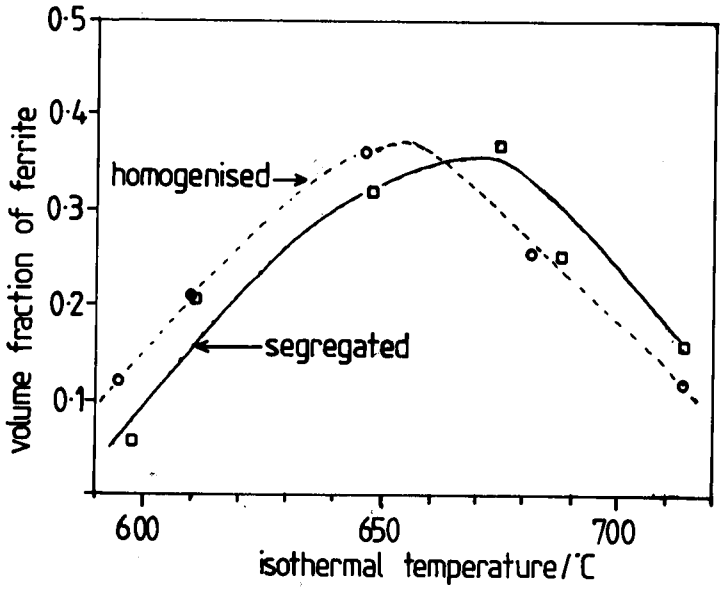


Figure 3.3. Ferrite volume fraction formed as a function of isothermal treatment temperature.

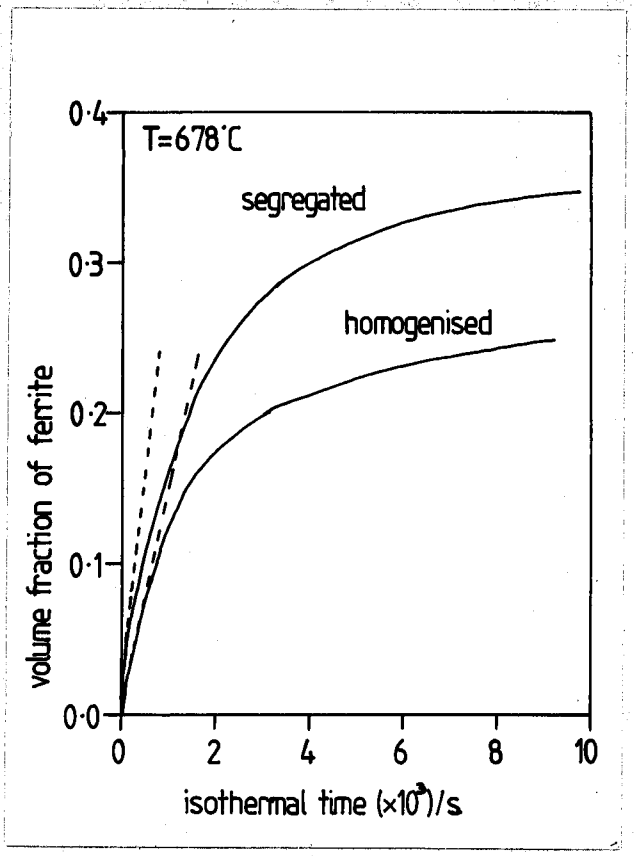


Figure 3.4. Transformation behaviour at 678°C.

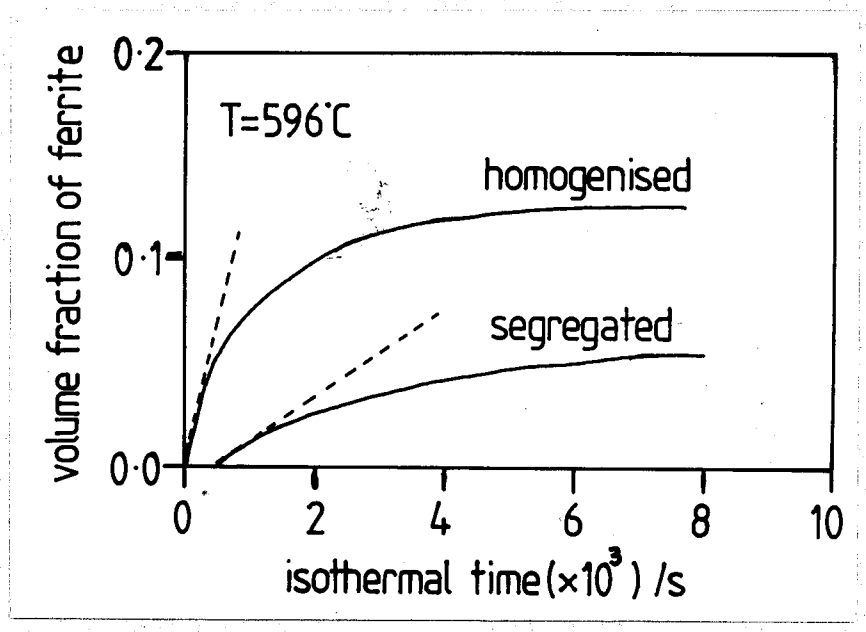


Figure 3.5. Transformation behaviour at 596°C.

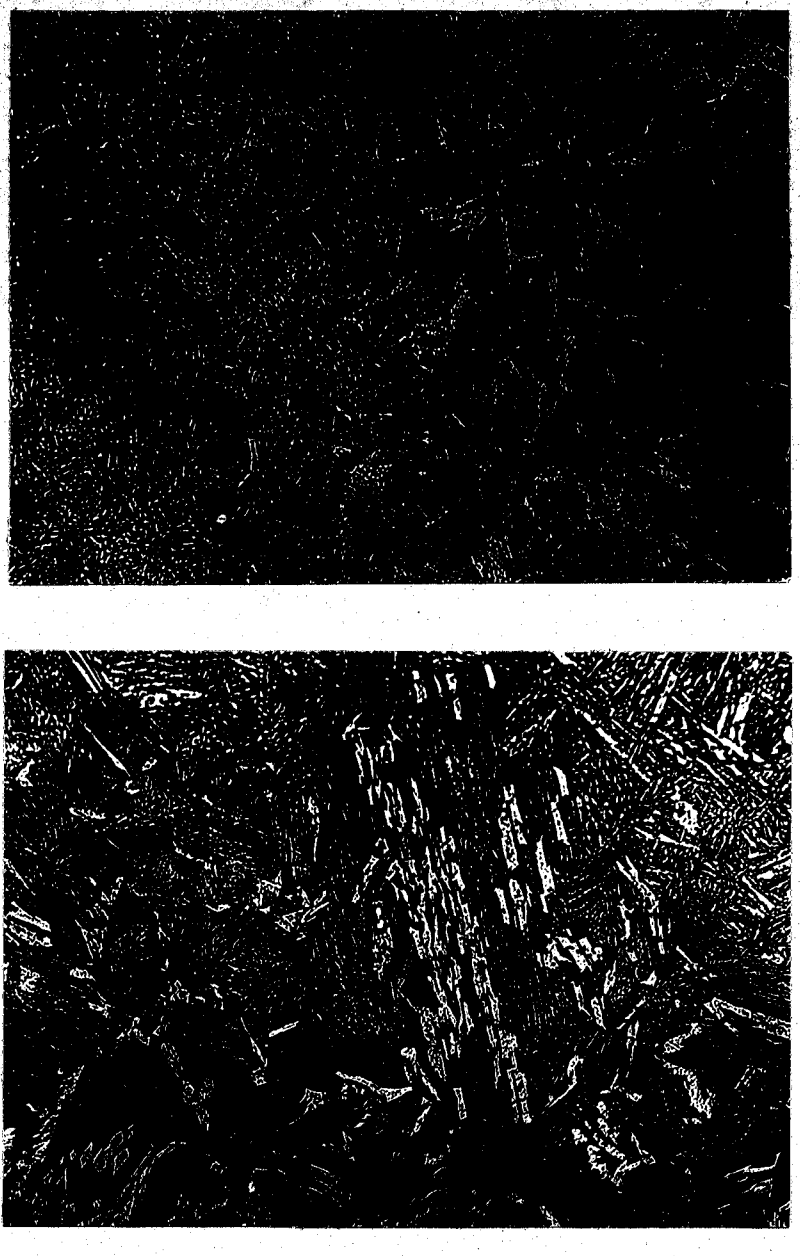


Figure 3.6. Microstructures for (a) segregated and (b) homogenised specimens isothermally heat treated for 30 minutes at 600°C after reaustenitisation at 1000°C for 10 minutes.

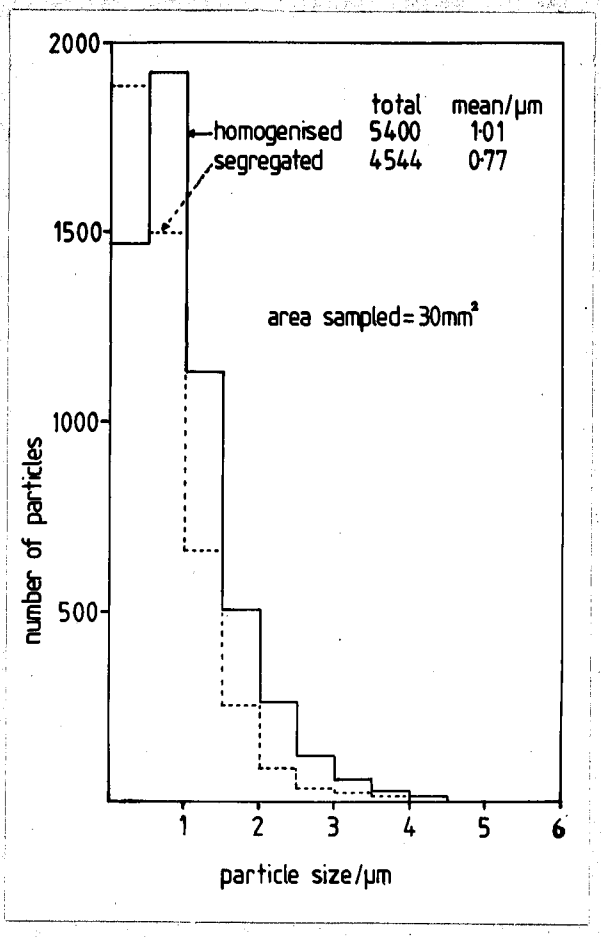


Figure 3.7. Particle counting results for ferrite allotriomorphs for specimens in fig. 3.6.

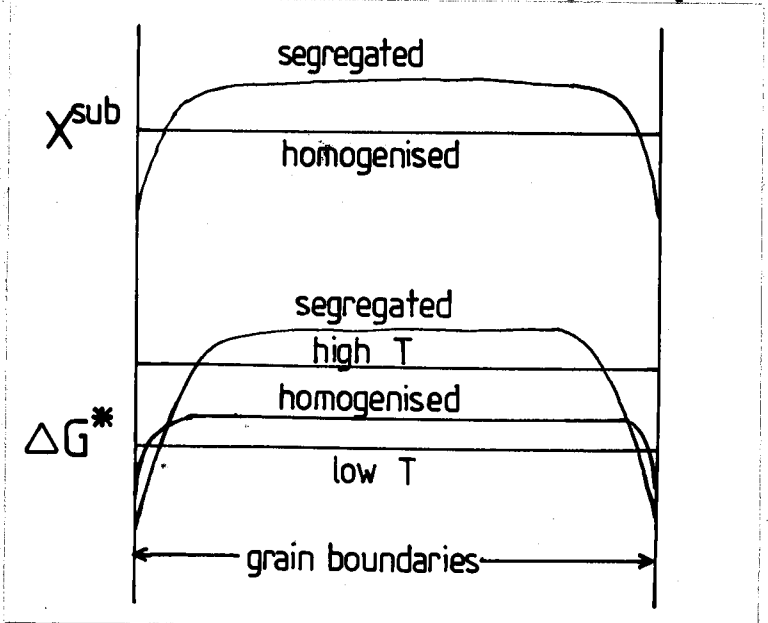


Figure 3.8. Variation of activation energy for nucleation across a grain for homogenised and segregated specimens.

# 4. The Mechanism of Acicular Ferrite Formation

## 4.1 Introduction

The general absence of acicular ferrite, a dense interlocking array of intragranularly nucleated ferrite plates, fig. 4.1, in wrought steels means that quantitative phase transformation theory has not been deduced for this phase. Substantial work on various effects on the formation of acicular ferrite ($\alpha_{acic}$) have been reviewed in chapter 2, but these have been carried out upon commercial or near commercial weld alloys, which have the drawback of transforming almost completely to ferrite. This hinders study of the mechanism of $\alpha_{acic}$ formation in two main ways:

(i) The microstructure of these welds contains a large volume fraction of ferrite composed of allotriomorphic $\alpha$, Widmanstätten $\alpha$ and $\alpha_{acic}$. The $\alpha_{acic}$ is generally a dense interlocking network of plates and the high volume fraction results in large scale hard impingement of the ferritic products. This causes the true morphology of the $\alpha_{acic}$ plates to be masked.

(ii) The large extent of transformation in these low carbon alloys means that the amount of retained austenite ($\gamma$) is low. This amount is generally insufficient to allow a detailed study of the parent $\gamma$/product $\alpha_{acic}$ relationship and interface.

In order to overcome these problems a series of welds of higher alloy content were prepared, the final compositions being given in Table IV.1. In order to be compatible with previous work the conditions of welding were standardised as in table IV.2.

The alloying additions were chosen in order to provide a high hardenability so that the degree of transformation was reduced whilst still retaining an essentially acicular microstructure. The high silicon levels were chosen to reduce any tendency for carbon enriched austenite to precipitate carbides and so increase the amount of austenite retained at room temperature. The smaller amount of transformation leads to less impingement so that the true morphology of the plates may be determined. In addition, the amount of austenite retained to room temperature ($\gamma_r$) was increased allowing detailed crystallographic studies of the $\gamma/\alpha_{acic}$ relationship to be performed.

## 4.2 As-deposited Microstructure

Fig. 4.2 shows the as-deposited (top bead) microstructure of the five welds (PJ303,4,5,6 & PJ495), which, with the exception of PJ495, contain a small amount of allotriomorphic ferrite, a few Widmanstätten $\alpha$ sideplates and a relatively open $\alpha_{acic}$ network, i.e. one with limited plate-plate contact. The amount of microphases was high and comprised a high proportion of retained $\gamma$. PJ495 was too highly alloyed and gave a fully martensitic microstructure due to the exceptional level of hardenability. This weld was not used further in this study. Of the other welds PJ304 and

306 had similar compositions and seemed most promising from a microstructural point of view so that extensive investigation of these specimens was performed.

3mm diameter rods were machined from the low dilution capping run of PJ304 & 306 and slit under flood lubrication to discs. These discs were ground to a thickness of 0.075mm prior to electropolishing and examination in a Philips 400T transmission electron microscope (TEM) operating at 120 kV. Foil preparation using 5% (by volume) perchloric acid, 25% glycerol, 70% ethanol electrolytes were unsatisfactory, with a narrow range between etching and pitting of the foil. This resulted in thickness variations, which caused problems with focus and contrast in the TEM images and arose mainly from the presence of large non-metallic inclusions. The use of below ambient temperatures to improve polishing was prohibited by the need to avoid transformation of the austenite to martensite and so ambient temperatures were used throughout. A reasonably successful electrolytic solution was found to be 5% perchloric acid in 95% acetic acid at voltages between 80V, when the solution was fresh, and 25V, when the solution was 1-2 months old.

### 4.3 Morphology

Bright field images of these foils (fig. 4.3) revealed that acicular ferrite plates were in fact lenticular which would be consistent with a thin plate morphology when extended to three dimensions. Detailed examination reveals each plate to be singular with no evidence of self accommodating pairs of plates as might be expected for Widmanstätten $\alpha$[170]. However, the plates were not devoid of sub-structure and some examples were observed of "sub-units" (fig. 4.4), which were also lenticular units of ferrite surrounded by retained austenite and were similar to those seen in ferrous bainites, especially in high Si steels [142].

The presence of Si prevents the precipitation of cementite from carbon rejected into the $\gamma$ by the ferrite so that $\gamma$ is retained to delineate the "sub-units". The chemically heterogeneous nature of weld metal and transformation over a range of temperatures during continuous cooling gives rise to $\alpha_{acic}$ plates that formed at lower temperatures and contain carbides towards the edge of the plate, fig. 4.5. These carbides, identified as $Fe_3C$, were in one orientation in each plate, often at $\approx 60°$ to the plate's long axis, and bear a strong resemblance to carbides observed in lower bainite [141]. The carbides were contained entirely within the ferrite and did not extend into $\gamma$ or along the interface, suggesting they precipitated from ferrite in the plate that was supersaturated with respect to carbon. The $\alpha_{acic}/\gamma$ interface was generally smooth and the occurrence of facets or ledges was not widely seen - only one or two examples, fig. 4.6. Their presence would not indicate the transformation mechanism, only the method of interface motion adopted and does not even indicate if the ledges contributed to the migration of the interface. The low occurrence of ledges suggests that interface motion by a ledge mechanism is not important. The smooth curvature of the plate extended to the tip, which was rounded (fig. 4.7), typical tip radii being 0.01-0.05μm. The tip radii were determined from measurements on around 85 plate tips from

several foils, by tangent constructions at and near the tip. Radii from these tangents intersect in the plate at the centre of curvature of the tip, from which the radius of the tip region can be measured. However, no stereological corrections were made and so the values quoted are only the apparent radii. The sample could not be considered completely random as the weld samples have an overall texture and the foils were obtained from specimens similarly oriented with respect to the weld. The dimensions of the same plates, when examined on a Quantimet 720 were length 3-10μm and width 1-3μm. This would give an apparent aspect ratio of around 3, although this is probably a large overestimation due to sectioning and stereological effects. Indeed, the optical microstructure (fig. 4.2) shows aspect ratios of the order of 10. Fig. 4.8 plots the aspect ratios recorded, along with their frequency of occurrence and plate length.

### 4.4 Surface Relief

In order to determine the nature of any surface relief associated with the formation of $\alpha_{acic}$, a specimen was prepolished to a 1μm diamond paste finish, thoroughly degreased and sealed in a quartz tube. Before final sealing the tube was flushed seven times with argon, pumped down to $10^{-6}$ torr and back filled with a partial pressure of argon to ensure a very low chance of oxide formation. The sample was then reaustenitised at 1300°C for 30 minutes to give a large $\gamma$ grain size to promote $\alpha_{acic}$ over grain boundary nucleated phases. The tube, still intact, was then plunged into iced water to give rapid cooling without oxidation. Nomarski interference microscopy was then carried out to reveal the surface relief, the size of the $\alpha_{acic}$ plates being too fine to use quantitative Tolanski measurements. As fig. 4.9 indicates, the transformation results in surface tilting which causes interference colours due to variations in the optical path length. Closer examination demonstrates that the contrast is uniform for each plate indicating that a uniform tilting occurs for each $\alpha_{acic}$ plate. The uniform contrast is consistent with an invariant plane strain (IPS) with a significant shear component. Scratches could not be resolved optically, which would have been another way of deducing the IPS nature of the strain. Gentle polishing of the surface and light etching revealed the microstructure underlying the relief (fig. 4.10) which was mostly $\alpha_{acic}$, hence the relief arrowed in 4.10a results from the $\alpha_{acic}$ plate in 4.10b and not from other displacive transformations such as grain boundary bainite or Widmanstätten $\alpha$ side plates. Further specimens were observed on a Camscan S4 scanning electron microscope, where the use of slight tilting gave stereo pairs. From these the dimensions of the tilted region could be determined and hence an estimate made of the associated strain energy. Unfortunately, the degree of surface tilting was limited so that accurate measurements of the surface relief were not possible. Thermal etching of dislocations gives rise to the circular features seen in figures 4.9 and 4.10, which also resulted in a low number of reliefs suitable for tilting. In order to get an estimate of the strain energy associated with surface relief the angle of the habit plane to the free surface needs to be known. This could not be determined in the SEM, but the habit planes should give a wide range of angles to the surface. If sufficient values of surface relief were available, an

estimate of the true strain energy could be obtained from the largest value as this corresponds to the situation when the habit plane is most nearly perpendicular to the free surface.

### 4.5 Crystallography

One of the greatest aids to deducing phase transformation mechanisms is the crystallographic relation between parent and product phases, in this case $\gamma$ around $\alpha_{acic}$ plates. Samples from the capping run of PJ304 contained sufficient $\gamma_r$, usually as a thin layer (fig. 4.11), to allow selected area diffraction patterns (SADP) to be taken from both phases simultaneously - after suitable tilting. The resulting patterns appear as in fig. 4.12, where the two zones (for $\alpha$ and $\gamma$) are outlined. Dark field imaging, fig. 4.13, was used to confirm the presence of $\gamma_r$ and identify those spots in the SADP corresponding to that phase. The diffraction patterns were then analysed to determine the crystallographic relationship between the austenite and acicular ferrite lattices. From each SADP a plane and direction were indexed for each plane; (hkl) and [uvw] for $\alpha$, $(h_1k_1l_1)$ and $[u_1v_1w_1]$ for $\gamma$, as shown in fig. 4.14. The two planes (hkl) and $(h_1k_1l_1)$ form a right handed set, as do the directions $[u_1v_1w_1]$ and [uvw]. The acute angle, $\phi$, between $(h_1k_1l_1)$ and [uvw] was also measured and matrix algebra used to determine the lattice relationship from these data. The initial step is to calculate the rotation matrix between the lattices from the axis/angle pair. The 111 and 011 vectors of one lattice were transformed into the co-ordinates of the other and the angle between 111 of one lattice and the nearest 011 of the other was calculated. This was then repeated for all possible <111>, <011> pairs to give the smallest angle between a 111 vector of one lattice and a 011 vector of the other. The vectors represent the closest packed planes and directions in the two lattices and the angles represent the deviations of the lattices from the exact Kurdjumov-Sachs (K-S) orientation relationship. The results for 32 incidents of co-existing acicular ferrite and austenite are listed in Table IV.3. *For all cases* observed the rotation required to bring the closest packed planes and directions into coincidence did not exceed 10°. Any lattice transformation achieved by a displacive mechanism involving deformation of the parent lattice to give the product lattice means that the two lattices must always be intimately related [78]. With regard to steels, the $\gamma$-$\alpha$ transformation is achieved by the Bain strain, a homogeneous deformation that introduces rotations of less than 11° [171-173] around the Bain orientation. Thus any displacive transformation must give an orientation relationship within 11° of the Bain orientation, i.e. within the Bain region, which also encompasses the K-S and Nishiyama-Wasserman orientation relationships. The experimentally determined orientation relationships are therefore consistent with a displacive transformation mechanism.

At the same time, the nature of the $\alpha/\alpha$ grain boundaries between plates of acicular ferrite was investigated and could be differentiated into two groups:

(i) High angle boundaries, with no special relation between the two ferrite lattices. These were often associated with larger dislocation densities in the plates, which resulted from physical impingement of plates originating from separate nucleation sites, fig. 4.15.

(ii) Special boundaries, in which the lattices are more closely related. These were typically coincident site lattices (CSL), where if one lattice is hypothetically extended across the boundary into the neighbouring grain a certain fraction of lattice sites in both lattices match, or are *coincident*. These CSL interfaces are characterised by $\Sigma$ values, where

$\Sigma$=reciprocal density of coincident sites

i.e. if one third of the lattice sites give perfect matching between the two crystals, then $\Sigma$=3. The matching of a certain number of sites across a boundary reduces the excess energy associated with the boundary as it approximates more closely to an extension of the crystal.

The latter type were frequently noted at $\alpha_{acic}$ plate interfaces at inclusions where multiple plate nucleation had occurred, fig. 4.16. CSL orientation relations were also observed when a second plate was found emanating from another plate away from an inclusion, fig. 4.17, but with a much lower apparent dislocation density than for (i). Although a full g.b analysis was not performed on the dislocations between hard plate impingements, these regions exhibited much higher dislocation densities even on tilting of the specimen. This was taken to indicate a higher density of dislocations in these regions. For CSL lattice relations the dislocation density adjacent to the second plate on tilting was not significantly greater than that in the rest of the plate. These were noted especially in reheated specimens quenched to capture the initial stages of $\alpha_{acic}$ formation, fig. 4.18. These effects are more likely to result from sympathetic nucleation of secondary plates on preexisting plates, than from physical impingement of growing plates. This process, in respect of $\alpha_{acic}$ formation, was first suggested by Ricks et al. [65] and the subject of sympathetic nucleation has recently been reviewed by Menon & Aaronson [174]. Initial nucleation is seen to be upon inclusions, presumably oxides, (fig. 4.19), but multiple nucleation on inclusions was often seen, as was plate nucleation upon other plates. This did not agree with the suggestion of Abson [175] that there was a one-to-one correspondence of nucleating inclusions and $\alpha_{acic}$ plates, i.e. each plate is nucleated by one inclusion and the limiting $\alpha_{acic}$ plate size and volume fraction is determined by the total number of inclusions present. The operation of sympathetic nucleation, after initial inclusion nucleation, generates the interlocking network through the successive nucleation of $\alpha_{acic}$ plates upon each other at different orientations until impingement occurs or the final volume fraction is reached. The maximum volume fraction and size of $\alpha_{acic}$ plates may then be controlled by the thermodynamics of the system rather than the total inclusion content.

### 4.6 Habit Plane

The $\gamma/\alpha_{acic}$ interface plane was indexed to ascertain whether a consistent irrational habit plane exists between the two phases. This was achieved by use of single surface trace analysis performed on corresponding TEM bright field images and diffraction patterns. The $\alpha_{acic}$ interface has been noted to curve gently so that there is a continuous variation in the interface plane along its length; however a substantial portion of this can be represented by a

single mean plane parallel to it (fig. 4.20). The lens optics used in TEM result in a rotation of the image between bright field and diffraction modes; this was calibrated over a range of magnifications and camera lengths by use of a $MoO_3$ crystal, which had facetted surfaces of known indices. Identifying the mean straight interface trace as the habit plane, the trace analyses, on some 90 plates, were carried out as follows, fig. 4.21:

(i) The normal, $\underline{n}$ (hkl), to the trace is marked on the bright field image.

(ii) The indexed diffraction pattern is then placed upon the bright field and rotated into coincidence (as determined from the calibration).

(iii) The angles ($\theta_i$) of the trace normal, $\underline{n}$, from two $\underline{g}$ vectors in the diffraction pattern are measured.

(iv) The two $\underline{g}$ vectors are used to calculate the zone axis, [UVW].

(v) The indices of $\underline{n}$ are determined.

It is unlikely that the $\gamma/\alpha_{acic}$ interface will be normal to the plane of the bright field, i.e. parallel to the zone axis, but is more likely to be at an angle $\phi$ to it. However, its true normal (HKL) must lie on the great circle defined by the measured trace normal (hkl) and the zone axis of the diffraction pattern [UVW]. The habit plane is therefore defined by the intersection of these great circles on a stereogram, but, as seen in fig. 4.22, this approach becomes increasingly more congested and inaccurate the more circles that are added. Therefore, a second approach was adopted, the normal to the habit plane should be at 90°to <u>all</u> the normals to these great circles. Hence the plane that minimises the deviations from orthogonality will be closest to the true habit plane, if such exists. Various proposed habit planes were selected and the deviations from the experimental great circle normals calculated (table IV.4). These results indicated that the best habit plane was close to $\{3\ 10\ 15\}_\gamma$ which is a well known martensite habit plane, but the mean deviation for $\{5\ 8\ 5\}_\gamma$ which is associated more with Widmanstätten $\alpha$ is greater. In addition the habit plane was calculated from the phenomenological theory of martensite formation as proposed by McKenzie and Bowles [176] and Wechsler, Liebermann and Read [177]:

*4.6.1 Phenomenological Theory of Martensite Crystallography*

The characteristics of a martensitic transformation include a shape deformation, which, macroscopically, has invariant plane strain (IPS) characteristics. The invariant (i.e. undistorted and unrotated) plane of the shape deformation is the habit plane of the martensite. As $\alpha_{acic}$ exhibits IPS surface relief then its formation will involve a habit plane, which is unaffected by subsequent partition of interstitial carbon. EDS microanalysis (section 4.8) reveals no partition of substitutional alloying elements.

The martensitic transformation from an FCC to BCC lattice requires the action of an invariant-line strain (ILS), i.e. one that leaves one direction in the parent lattice unrotated and undistorted in the product lattice. This can be represented in matrix notation [178,179], also appendix 1, as (F S F). The change from an FCC to BCC lattice can be achieved by the Bain strain, fig. 4.23, (F B F), which involves elongations along $\langle 110\rangle_\gamma$ and $\langle \bar{1}10\rangle$ and a contraction along $\langle 001\rangle_\gamma$. This does

not give an ILS and must be combined with a rigid body rotation (F J F) to give the required ILS:

$$(F\ S\ F)=(F\ J\ F)(F\ B\ F)$$

This can be thought of as the operation of two invariant-plane strains (IPS), fig. 4.24. It must be stressed that this is merely a mathematical device and does not imply anything about the sequence of strains in the transformation, which must take place simultaneously.

The initial strain, (F P F), fig. 4.24a-4.24b, is that producing the macroscopic shape deformation, defining the habit plane (unit normal $\underline{p}$), magnitude m of shape deformation and unit deformation vector $\underline{d}$. However, this IPS does not result in the correct product lattice only in some intermediate lattice. A second IPS (F Q F), fig. 4.24b-4.24c, is required to generate the correct lattice with the action of the two IPS's amounting to an ILS. This combination produces the correct lattice, but incorrect shape deformation, hence a lattice invariant deformation (inhomogeneous slip or twinning) must act to generate the final product shape, fig. 4.24c-4.24d or 4.24e.

*4.6.2 Prediction of Habit Plane*

The possibility of carbon partition after the displacive formation of ferrite means that measurement of the lattice parameters at room temperature by TEM or X-ray diffractometry will not represent those at transformation, even allowing for thermal expansivities. Hence, the lattice parameters were estimated using formulae derived by Dyson and Holmes [169] and Leslie [180], for the bulk composition, including full carbon content. The substitutional alloying element concentrations were determined by EDS on thin foils.

The smallest atomic displacements during transformation between FCC and BCC lattices occur for the Bain strain and this correspondence was assumed between the lattices so that

$$(F\ B\ F) = \begin{pmatrix} \eta_1 & 0 & 0 \\ 0 & \eta_1 & 0 \\ 0 & 0 & \eta_3 \end{pmatrix}$$

where the principal strains $\eta_1$ and $\eta_3$ are determined from the lattice parameters of ferrite ($a_\alpha$) and austenite ($a_\gamma$).

A second assumption is made about the invariant line of the lattice deformation in that it must lie in $(101)_\gamma$ and its plane contains $[10\bar{1}]_\gamma$. This is effectively assuming slip is on the system

$$(101)_\gamma[10\bar{1}]_\gamma \equiv (111)_\alpha[11\bar{2}]_\alpha$$

The invariant line, referred to the orthonormal basis F is

$$[F;\underline{u}]=[u_1\ u_2\ u_3]$$

where for $\underline{u}$ to lie in $(101)_\gamma$ $u_1+u_3=0$

In austenite

$$|\underline{u}|^2=(\underline{u};F)[F;\underline{u}]=1$$

The lattice deformation results in $\underline{u}$ becoming the vector $\underline{w}$ in ferrite, which, when referred to the same basis, gives

$$|\underline{w}|^2=(\underline{w};F)[F;\underline{w}]$$

but $\underline{u}$ and $\underline{w}$ are related by the deformation matrix (F B F) so that

$$|\underline{w}|^2=(\underline{u};F)(F\ B\ F)^2[F;\underline{u}]$$

If $\underline{u}$ is the invariant line then

$$|\underline{u}|^2=|\underline{w}|^2$$

$$u_1^2+u_2^2+u_3^2=\eta_1^2u_1^2+\eta_1^2u_1^2+\eta_3^2u_3^2$$

leading to the matrix equation

$$\begin{pmatrix} 1 & 1 & 1 \\ 1 & 0 & -1 \\ (\eta_1^2-1) & (\eta_1^2-1) & (\eta_3^2-1) \end{pmatrix} \begin{pmatrix} u_1^2 \\ u_2^2 \\ u_3^2 \end{pmatrix} = \begin{pmatrix} 1 \\ 0 \\ 0 \end{pmatrix}$$

Solution of this leads to two possibilities for the set $u_1\ u_2\ u_3$

A similar process is now carried out for the plane defined by the invariant normal of (F S F), which in austenite is given by $h_1\ h_2\ h_3$, but on transformation to ferrite becomes $\underline{l}$. The deformation matrix (F B F) again relates $\underline{h}$ and $\underline{l}$ so that

$$|\underline{l}|^2=(\underline{h};F^*)(F\ B\ F)^{-1}(F\ B'\ F)^{-1}[F^*;\underline{h}]$$

Invariance also requires that

$$|\underline{h}|=|\underline{l}|$$

$$h_1^2+h_2^2+h_3^2 = \left(\frac{h_1}{\eta_1}\right)^2 + \left(\frac{h_2}{\eta_1}\right)^2 + \left(\frac{h_3}{\eta_3}\right)^2$$

and the matrix equation

$$\begin{pmatrix} 1 & 1 & 1 \\ 1 & 0 & -1 \\ \left(\frac{1}{\eta_1^2}-1\right) & \left(\frac{1}{\eta_1^2}-1\right) & \left(\frac{1}{\eta_3^2}-1\right) \end{pmatrix} \begin{pmatrix} h_1^2 \\ h_2^2 \\ h_3^2 \end{pmatrix} = \begin{pmatrix} 1 \\ 0 \\ 0 \end{pmatrix}$$

whose solution leads to two possible sets of values for $h_1$, $h_2$ and $h_3$.

This analysis gives two possible invariant lines and invariant normal planes and hence four ways of choosing pairs of undistorted lines and normals. Therefore by choosing one pair $\underline{u}$ and $\underline{h}$, the rigid body rotation matrix (F J F) needed to convert (F B F) into the ILS (F S F) can be found. From a consideration of the cross products of $\underline{u}$ and $\underline{h}$ and their BCC counterparts $\underline{w}$ and $\underline{l}$.

$$\underline{a}=\underline{u}\wedge\underline{h}$$

$$\underline{b}=\underline{w}\wedge\underline{l}$$

The action of (F J F) is to rotate $\underline{w}$ into coincidence with $\underline{u}$, $\underline{l}$ with $\underline{h}$ and $\underline{b}$ with $\underline{a}$, which is expressed by the equations

$$[F;\underline{u}]=(F\ J\ F)[F;\underline{w}]$$

$$[F;\underline{h}]=(F\ J\ F)[F;\underline{l}]$$

$$[F;\underline{a}]=(F\ J\ F)[F;\underline{b}]$$

or

$$\begin{pmatrix} u_1 & h_1 & a_1 \\ u_2 & h_2 & a_2 \\ u_3 & h_3 & a_3 \end{pmatrix} = \begin{pmatrix} J_{11} & J_{12} & J_{13} \\ J_{21} & J_{22} & J_{23} \\ J_{31} & J_{32} & J_{33} \end{pmatrix} \begin{pmatrix} w_1 & l_1 & b_1 \\ w_2 & l_2 & b_2 \\ w_3 & l_3 & b_3 \end{pmatrix}$$

From which the elements $J_{ij}$ of (F J F) can be found and the invariant-line strain deduced from

$$(F\ S\ F) = (F\ J\ F)(F\ B\ F)$$

In order to deduce the habit plane it is necessary to decompose the ILS (F S F) into its two component invariant-plane strains (F P F) and (F Q F).

(F P F) completes the shape deformation determining the habit plane (normal $\underline{p}$), shape deformation magnitude m and unit direction $\underline{d}$. This results in an intermediate lattice and is given by

$$(F\ P\ F)=I+m[F;\underline{d}](\underline{p};F^*)$$

The lattice change is completed by the second IPS, whose deformation has magnitude n on a plane with unit normal $\underline{q}$ in unit direction $\underline{e}$. This second deformation is later cancelled by the lattice invariant shear, which is assumed to be on $(101)_\gamma[\bar{1}01]_\gamma$ hence (F Q F) must be shear on $(101)_\gamma[\bar{1}01]_\gamma$

$$(F\ S\ F)=(F\ P\ F)(F\ Q\ F)$$
$$=\{I+m[F;\underline{d}](\underline{p};F^*)\}\{I+n[F;\underline{e}](\underline{q};F^*)\}$$

if $a=\det(F\ P\ F)$

and $\underline{b}=am(\underline{q};F^*)[F;\underline{d}]$

gives

$$b(\underline{p};F^*)=(\underline{q};F^*)-(\underline{q};F^*)(F\ S\ F)^{-1}$$

(F S F) is known, so that normalisation gives the habit plane $(p_1\ p_2 p_3)$.

An analysis of this type was performed for PJ304 and the results indicated that the most favourable habit plane, assuming a displacive reaction, was:

$$\{0.117\ \ 0.675\ \ 0.729\}_\gamma$$

A plane that, when tried, gave minimum deviation from orthogonality, Table IV.4, and is only 4.42° from $\{3\ 10\ 15\}_\gamma$

### 4.7 Transformation Rate

In order to assess the transformation rate of acicular ferrite, specimens of PJ306 were reaustenitised at 1200°C for 10 minutes and then He quenched to temperatures between 440 and 560 °C for various times. The high reaustenitising temperature ensured a large austenite grain size, which minimised the formation of allotriomorphic α during the quenches, although some was noted decorating the grain boundaries (fig. 4.25). Careful etching using 2% Nital combined with the use of 25 ASA film and high contrast photographic paper gave images with sufficient contrast between ferrite and microphases (mainly α′) to allow computer image analysis of the microstructure. This was carried out on a Quantimet 720 and allowed measurement of the

development of $\alpha_{acic}$ plates without the associated microphases. As noted above, this is not the standard practice as the volume fraction of $\alpha_{acic}$ often includes the microphase regions entrapped in the interlocking network. However, when considering the mechanism of $\alpha_{acic}$ transformation it is more valid as the microphases result from later lower temperature transformations after $\alpha_{acic}$ formation has ceased. The results from this are given in fig. 4.26 and illustrate the following points:

(i) The incubation time, the time before ≈ 5% of $\alpha_{acic}$ forms as this is the first noticeable volume fraction, is seen to be ≈ 30s, a time that is relatively independent of temperature over the range studied.

(ii) The transformation rate is extremely rapid at all temperatures with reaction ceasing after ≈ 100s.

This optical work was extended by a series of dilatometric experiments in which transformations were carried out around 520 - 560°C, where the volume fraction of $\alpha_{acic}$ was estimated from the length change recorded and confirmed by optical microscopy. The method of determining volume fraction of ferrite from the length change recorded in dilatometric experiments was given in chapter 3. Although high volume fractions of $\alpha_{acic}$ plates were recorded, the reaction never proceeded to completion and so the data were replotted as mole fraction of carbon in residual $\gamma$ versus isothermal temperature (fig. 4.27). There was no evidence of any carbide precipitation either in optical specimens or in later TEM studies of these specimens, which could invalidate these calculations. The mole fraction of carbon in austenite was derived by calculating the equilibrium mole fraction of carbon in $\alpha$ at the isothermal temperature and combining this with the volume fraction at cessation of the transformation to give $x_c^{\gamma}$ in the residual $\gamma$ at that temperature. This analysis has extremely important implications for the transformation mechanism as transformation is seen to be incomplete, stopping between $T_0$ and $T_0'$ rather than $Ae_3$ and will be discussed later. The $T_0$ curve represents the temperatures and carbon contents (of austenite) where $\gamma$ and $\alpha$ of the same composition have the same free energy and so displacive transformations have zero driving force and so do not take place. $T_0'$ represents the same situation , but taking into account the strain energy ($400Jmol^{-1}$ in this case) involved in the shear part of the transformation. As temperature decreases the $x_c^{\gamma}$ where reaction ceases shifts over towards $T_0'$.

### 4.8 Microanalysis

The distribution of substitutional alloying elements across an interface can be found quickly, with reasonable accuracy (±5-10% of the actual value) on a fine scale in a TEM by EDS methods. The electron beam in a standard TEM can be condensed down to ≈ 5nm in diameter, which , with beam interaction within the foil, gives a spreading of typically ≈ 25nm for a 100nm thick Fe based foil. The spreading depends to some extent on density of the material. The spatial resolution of this technique is limited by foil thickness and is only improved by preparing thinner

foils. The area sampled in the conventional TEM mode is therefore $\geq 500nm^2$. Beam diameter can be reduced by using a scanning transmission electron microscope (STEM) mode so that the area sampled is reduced to $\approx$ $50nm^2$ with good foils. The conventional mode was general fine enough for the purposes of this investigation as STEM is disadvantaged by poor image resolution and low count rates, which require long counting times and so may experience beam drift during sampling. Composition variations were determined along and across plates of $\alpha_{acic}$ and across the $\alpha_{acic}$/microphase interface for the major alloying elements Mn and Si (fig. 4.28). These traces indicate no consistent trend in substitutional alloying element concentration along a plate or across the $\alpha_{acic}/\gamma$ interface. In the latter case, the agreement for Mn is better than that for Si, because the $\alpha$ plates are thinner than the adjacent microphases and give rise to less absorption of the X-ray signals. This affects the X-rays from the lighter Si more than those from Mn. These data are of limited use as they only indicate whether partition has occurred or not. However, although a displacive transformation by necessity involves no partition, paraequilibrium and NP-LE - both of which can be diffusional in nature - also give no partition of substitutional alloying elements. Therefore the lack of partition in fig. 4.28 does not indicate that the transformation is displacive or diffusional but must be taken with the other evidence. Microanalysis can only deduce the transformation mechanism at low undercooling when partition occurs during diffusional P-LE growth.

## 4.9 Discussion

The results presented above are all consistent with a displacive type of phase transformation as they reveal following characteristics:

(i) Lattices intimately related by orientation relationships within the Bain region in all cases.

(ii) No bulk partitioning of substitutional elements.

(iii) Invariant-plane strain surface relief.

(iv) Consistent habit plane between $\alpha_{acic}$ and $\gamma$, which agrees with that predicted by the phenomenological theory of martensite crystallography.

(v) Lenticular morphology to minimise the effect of strain energy due to the shape deformation of the displacive transformation.

Thus $\alpha_{acic}$ can be viewed as a form of Widmanstätten $\alpha$ or bainite, both of which are displacive transformations, but which differ in the extent of carbon diffusion associated with the ferrite formation stage and their respective strain energies. As mentioned in chapter 2, the large strain energy associated with a displacive FCC-BCC transition is inconsistent with the low driving force ($\Delta T$) at which Widmanstätten $\alpha$ forms. This is reduced by the simultaneous back-to-back formation of two mutually accommodating plates, but carbon equilibrium must be maintained at the interface so the formation of Widmanstätten $\alpha$ is a carbon diffusion controlled displacive reaction. The effect of carbon redistribution during transformation is to allow the reaction to proceed until the composition of the residual $\gamma$ reaches that given by the $Ae_3'$ line, i.e. to allow

the paraequilibrium amount of $\alpha$ to form. In contrast, bainite forms as a single sub-unit with a much larger strain energy and consequently at much higher undercoolings, forming with a full supersaturation of carbon in ferrite. The full mechanism involves the displacive formation of a ferrite sub-unit from $\gamma$ with no composition change, even in carbon. The free energy change for this stage is illustrated in fig. 2.36. After formation of this sub- unit, which is lenticular to minimise strain energy, carbon redistribution takes place into the adjacent $\gamma$. In the upper bainite regime, where diffusion of carbon is fairly rapid, redistribution typically occurs in less than 0.1s. The next sub-unit to form does so in a carbon enriched matrix (fig. 2.36) and after its formation further carbon partition occurs. This occurs until the carbon enrichment of $\gamma$ causes $\gamma$ and $\alpha$ of the same composition to have the same free energy (fig. 2.36) and the transformation stops. This case defines the $T_0$ curve as drawn in fig 4.27 and represents the combination of temperature and $x_c^{\gamma}$ where the driving force for displacive $\gamma$-$\alpha$ transformation is reduced to zero. The $T_0'$ (also presented in 4.2?) represents the same condition but allowing for a certain amount of strain energy, which opposes the reaction. This is the incomplete reaction phenomenon exhibited by upper and lower bainite.

The points in fig. 4.27 for $\alpha_{acic}$ which fall between $T_0$ and $T_0'$ therefore indicate that $\alpha_{acic}$ is a form of bainite nucleated intragranularly, probably upon deoxidation products, rather than Widmanstätten $\alpha$. The swing towards $T_0'$ at lower temperatures could be due to the greater effect of strain energy at lower temperatures, where $\sigma_y$ increases, so that any plastic accommodation becomes more difficult, as does dislocation motion for any transformation. In opposition to this, an increased volume fraction could result from reduced carbon mobility, which means that subsequent sub-units form before full redistribution of carbon from previous sub-units has occurred. Hence the driving force for displacive transformations is greater than zero for longer, allowing more $\alpha_{acic}$ to form. The incomplete redistribution of carbon from the ferrite sub-units means they are still supersaturated with respect to carbon and gives rise to the precipitation of carbides within the sub-units, as seen in lower bainites. This will be pursued further in chapter 5.

Table IV.1. Final weld compositions (wt %, except O and N, ppm).

| Weld | C | Si | Mn | Ni | Mo | Cr | Ti | V | Al | S | P | O | N |
|---|---|---|---|---|---|---|---|---|---|---|---|---|---|
| PJ303 | 0.121 | 0.41 | 3.09 | 0.02 | 0.01 | 0.05 | 0.04 | 0.01 | 0.01 | 0.011 | 0.022 | 213 | 126 |
| PJ304 | 0.201 | 0.44 | 1.80 | 0.03 | 0.01 | 0.04 | 0.02 | 0.01 | 0.01 | 0.008 | 0.022 | 212 | 108 |
| PJ305 | 0.180 | 1.52 | 1.40 | 0.02 | 0.01 | 0.05 | 0.04 | 0.01 | 0.01 | 0.008 | 0.020 | 205 | 94 |
| PJ306 | 0.214 | 0.45 | 1.78 | 0.03 | 0.01 | 0.05 | 0.02 | 0.01 | 0.01 | 0.008 | 0.022 | 186 | 94 |
| PJ495 | 0.317 | 0.44 | 0.317 | - | - | - | - | - | - | 0.005 | - | - | - |

Table IV.2. Welding parameters used in preparation of PJ series.

| Joint Geometry | ISO 2560 |
|---|---|
| | (24 runs in 8 layers of 3) |
| Welding Speed | $2mms^{-1}$ |
| Welding Voltage | 23V(DC+) |
| Welding Current | 180A |
| Interpass Temperature | 250°C |

Table IV.3. Orientation relationship between $\gamma$ and $\alpha_{acic}$. $\theta$is the angle (degrees) between the closest packed planes of the two lattices, $\{111\}_{\gamma}$ and $\{011\}_{\alpha_{acic}}$. $\phi$is the angle between the corresponding close-packed directions $<0\bar{1}1>_{\gamma}$ and $<\bar{1}11>_{\alpha_{acic}}$.

| $\theta$ | $\phi$ | $\theta$ | $\phi$ | $\theta$ | $\phi$ |
|---|---|---|---|---|---|
| 6 | 6 | 6 | 6 | 3 | 3 |
| 10 | 10 | 8 | 8 | 7 | 7 |
| 0 | 8 | 0 | 0 | 6 | 6 |
| 6 | 6 | 7 | 7 | 5 | 5 |
| 5 | 5 | 0 | 2 | 0 | 0 |
| 3 | 7 | 6 | 6 | 6 | 6 |
| 2 | 2 | 7 | 7 | 0 | 0 |
| 4 | 4 | 0 | 0 | 4 | 4 |
| 0 | 0 | 10 | 10 | 0 | 0 |
| 10 | 10 | 9 | 9 | 7 | 7 |
| 9 | 9 | | | | |

Table IV.4. Mean deviation, $\delta$(degrees), of habit plane normal from orthogonality for all single surface trace analyses.

| hkl | $\delta$ | hkl | $\delta$ |
|---|---|---|---|
| 1 1 0 | 10.9 | 4 3 3 | 9.80 |
| 3 2 1 | 4.72 | 3 1 1 | 6.08 |
| 5 3 2 | 5.14 | 4 1 1 | 5.83 |
| 1 1 1 | 12.82 | 3 10 15 | 4.19 |
| 2 1 2 | 6.59 | 3 4 5 | 7.67 |
| 3 1 3 | 5.45 | 5 5 8 | 9.33 |
| 4 1 4 | 5.13 | 28 10 13 | 5.34 |
| 1 0 0 | 18.13 | 2 1 1 | 7.80 |
| 3 2 2 | 9.06 | | |

Predicted habit planes.

| hkl | | | $\delta$ |
|---|---|---|---|
| 0.7081 | 0.1056 | 0.6982 | 4.84 |
| 0.7280 | 0.1171 | 0.6747 | 3.98 |

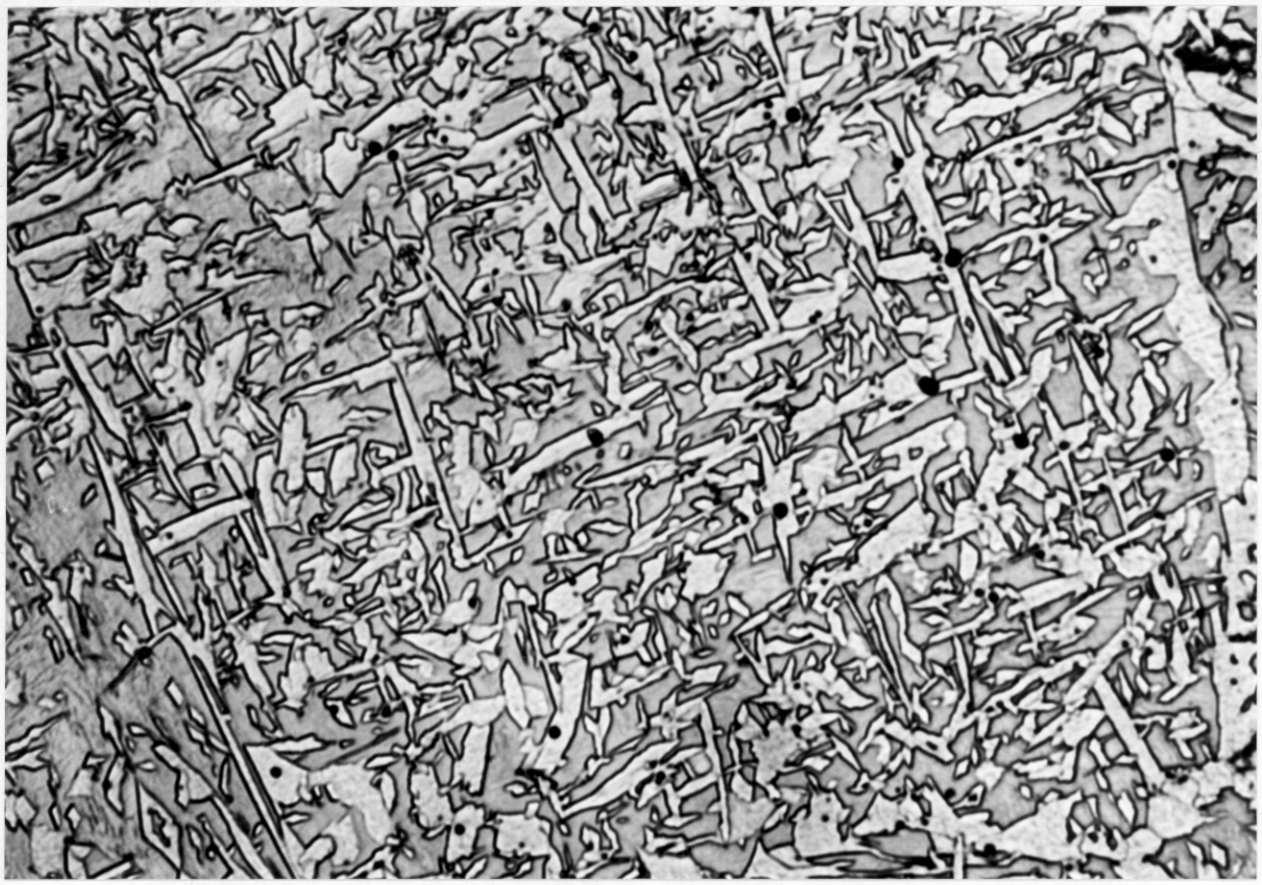

Figure 4.1. 0.7μm Star shaped formations typical of acicular ferrite.

(a) 15μm

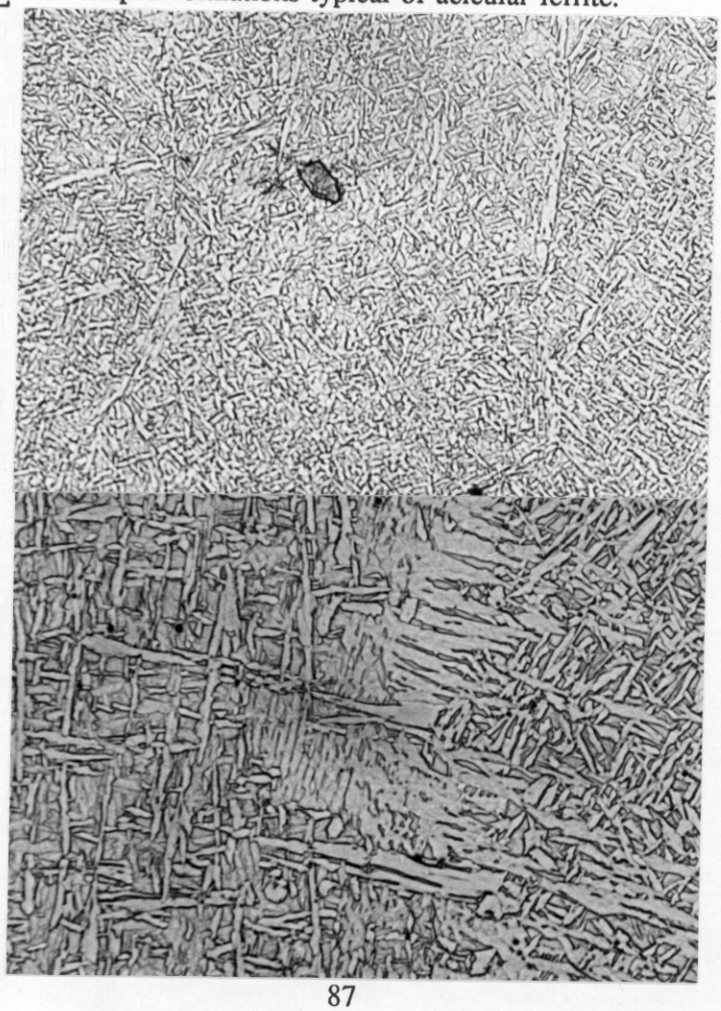

(b) 10μm

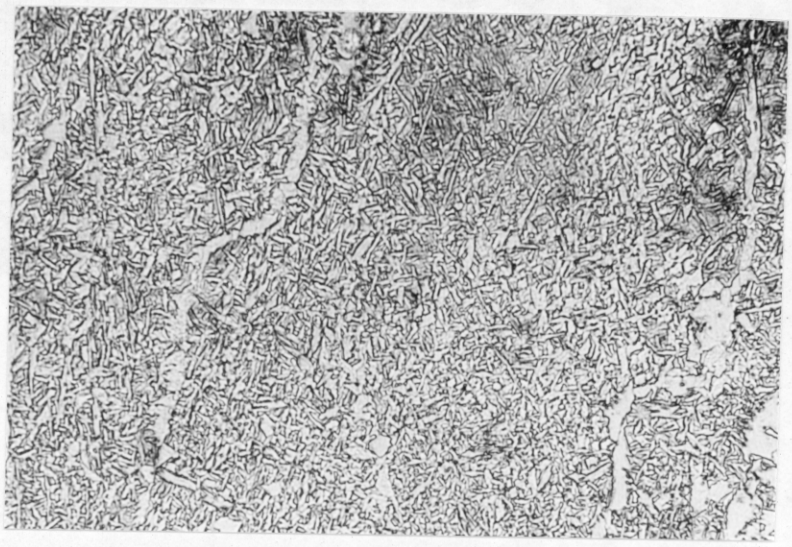

(c) 20μm

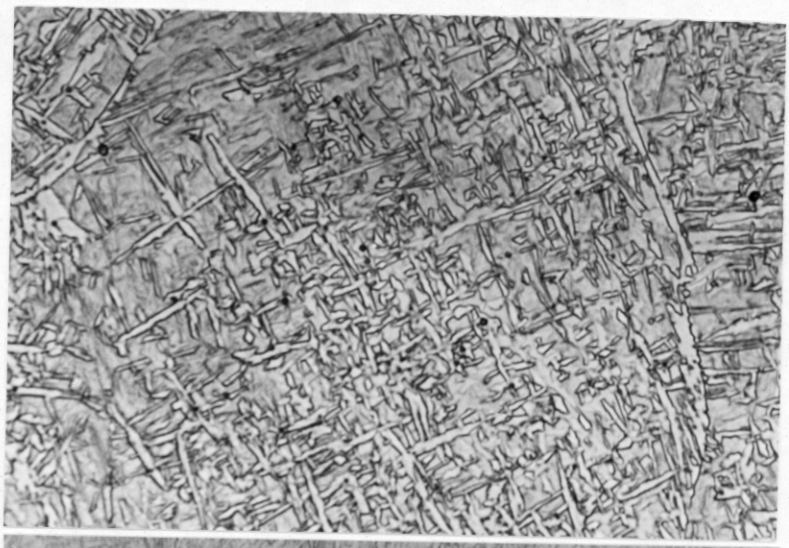

(d) 10μm

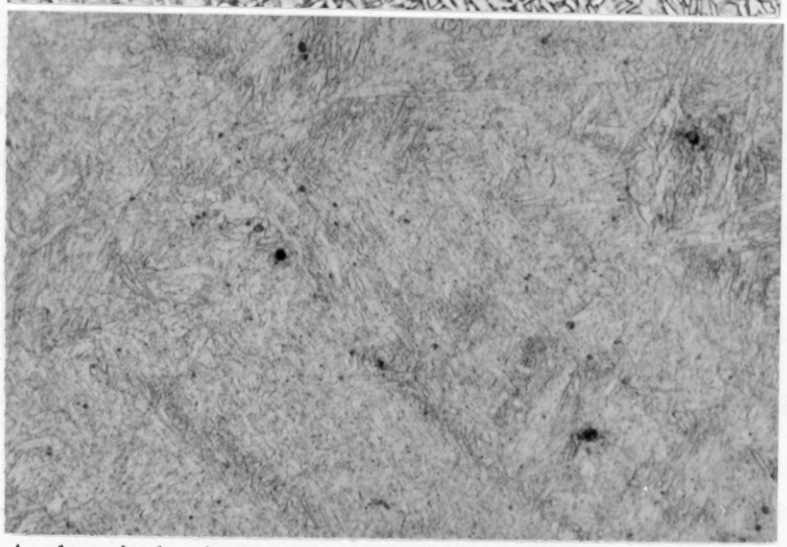

(e) 15μm

Figure 4.2. As-deposited microstructures, (a) PJ303, (b) PJ304, (c) PJ305, (d) PJ306, (e) PJ495.

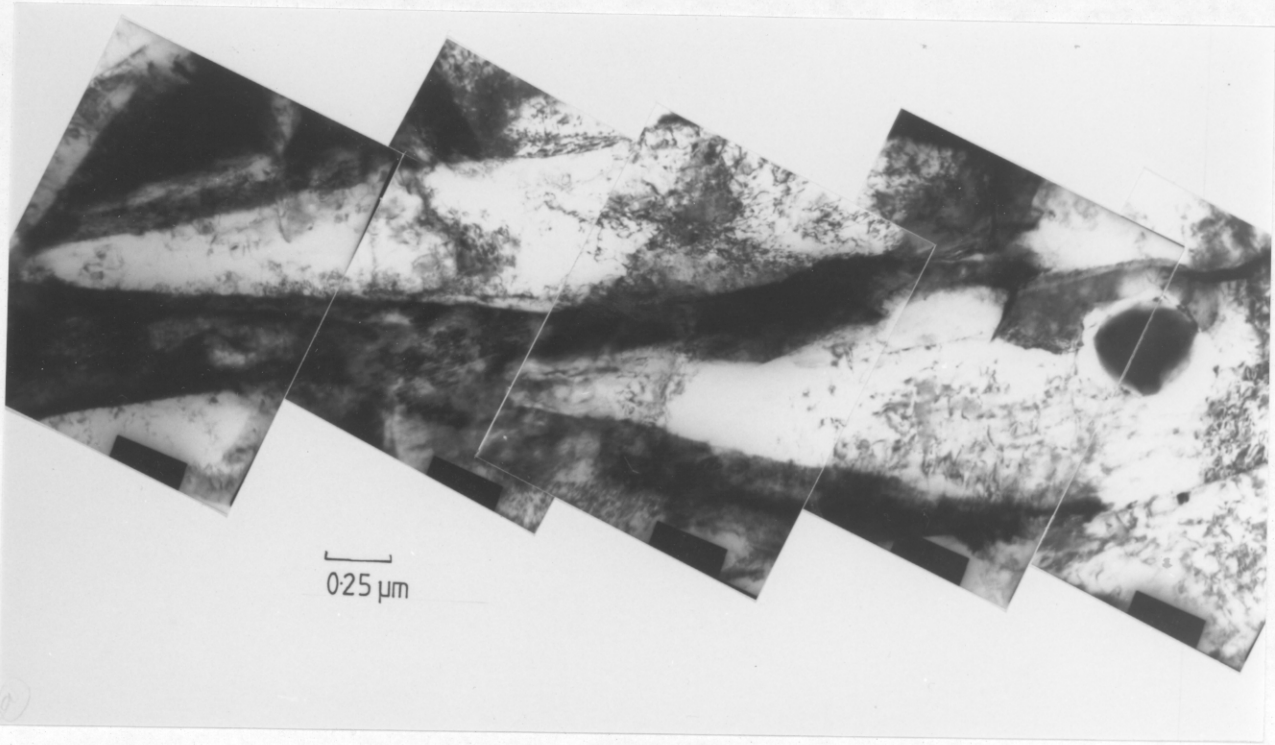


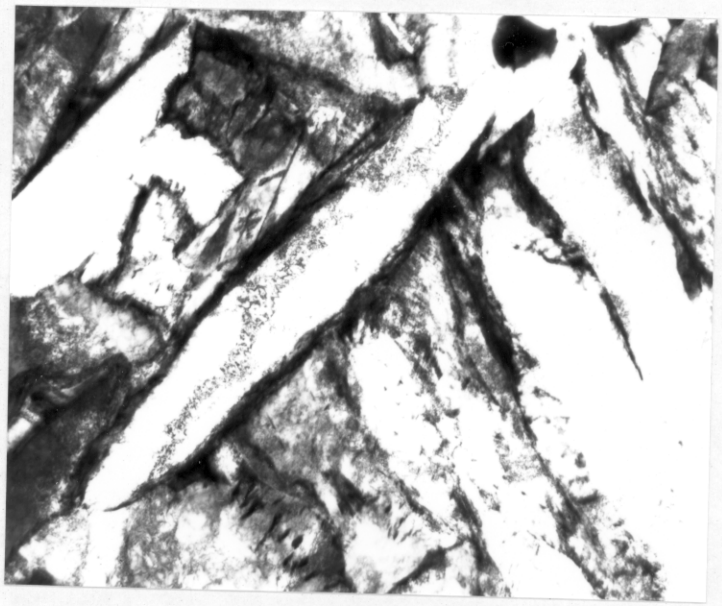

0.5µm

Figure 4.3. Lenticular acicular ferrite plates in as-deposited PJ304.

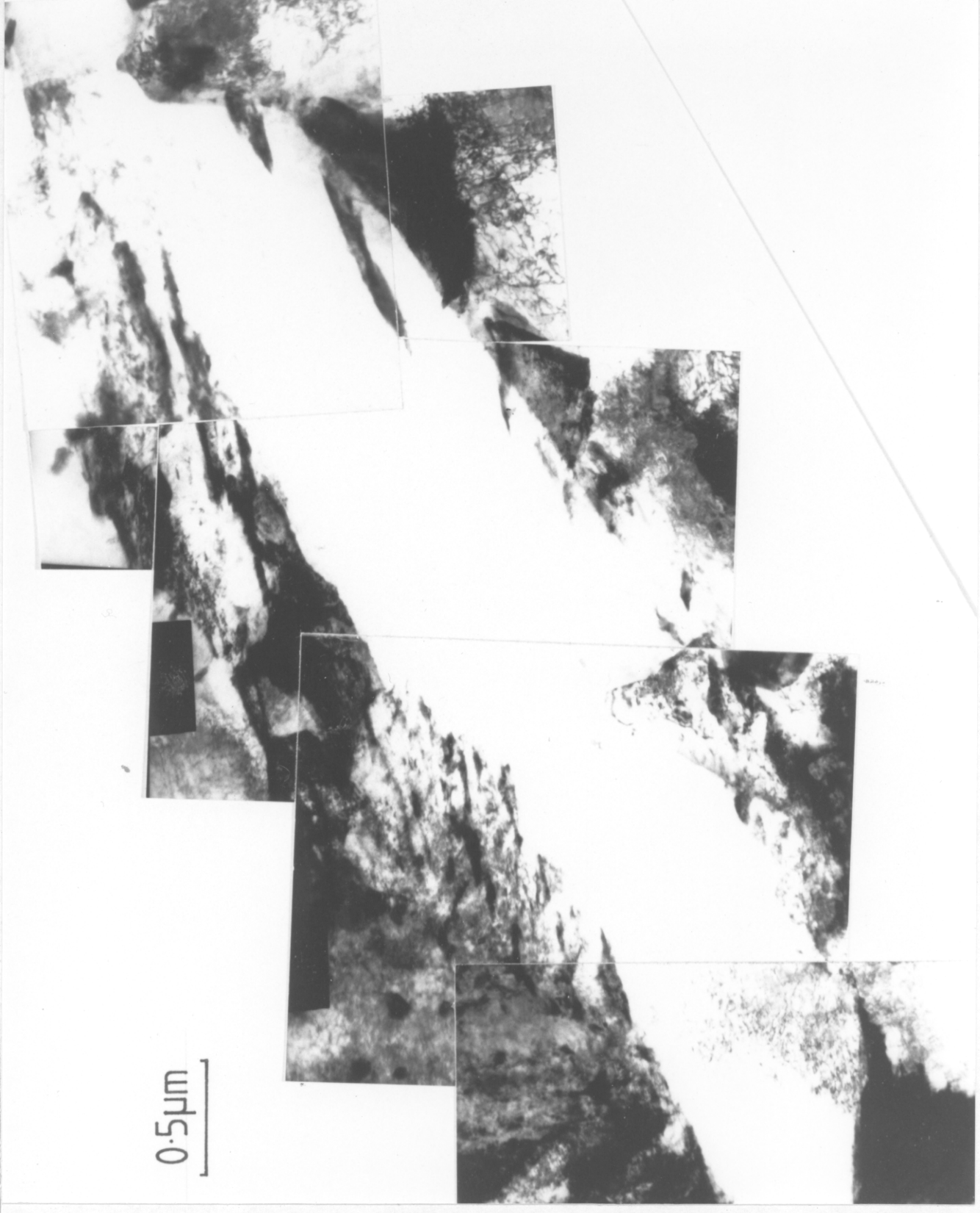


Figure 4.4. Ferritic sub-units, delineated by retained austenite, in an acicular ferrite plate.